Materials & Design 226 (2023) 111668

Contents lists available at ScienceDirect

Materials & Design

journal homepage: www.elsevier.com/locate/matdes

Analysis of position-dependent cavity parameters in irradiated metals to obtain insight on fundamental defect migration phenomena ☆

Yan-Ru Lin [a,b,*], Arunodaya Bhattacharya [a,d], Steven J. Zinkle [a,b,c]

[a] Materials Science and Technology Division, Oak Ridge National Laboratory, Oak Ridge, TN 37831 USA
[b] Department of Material Science and Engineering, University of Tennessee, Knoxville, TN 37996, USA
[c] Department of Nuclear Engineering, University of Tennessee, Knoxville, TN 37996, USA
[d] United Kingdom Atomic Energy Authority, Culham Centre for Fusion Energy, Culham Science Centre, Abingdon, Oxford OX14 3DB, United Kingdom

HIGHLIGHTS

- Bubble formation was observed within the void-denuded zones, indicative of a small bubble-denuded zone compared to the void-denuded zone.
- Enhanced cavity swelling regions adjacent to void-denuded zones were observed by planar sinks in samples with moderate sink strengths.
- The temperature dependence of the cavity-denuded zone could be used to quantitatively estimate defect (vacancy and He-vacancy complex) migration energies.
- Radiation-enhanced diffusion together with thermal diffusion can broaden the implanted ion profile and reduce the midrange safe analysis region.
- Sufficiently high ion energies are generally needed to provide an adequate safe analysis region for heavy ion irradiation effects studies.

GRAPHICAL ABSTRACT

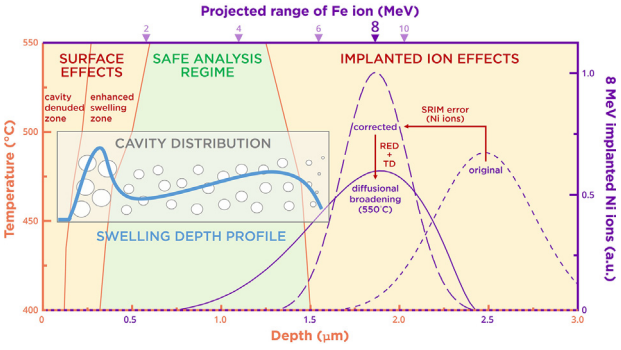

ARTICLE INFO

Article history:
Received 22 November 2022
Revised 18 January 2023
Accepted 27 January 2023
Available online 28 January 2023

Keywords:
Irradiation effects
Void/cavity denuded zone

ABSTRACT

Motion of point defects is a fundamental process that governs microstructure and properties of materials. Here, we examine the near-surface and grain boundary cavity swelling depth profiles in neutron- and ion-irradiated simple metals (Cu, Ni, and Fe-Cr) and investigate diffusional broadening of implanted Ni ions in Fe-Cr alloys. Vacancy migration energies and radiation-enhanced diffusion were experimentally estimated. Cavity denuded zone widths near planar sinks are shown to be dependent on temperature, damage rate, balance of point defects and sinks, and vacancy migration energies. An enhanced cavity swelling zone adjacent to the void-denuded zone was observed in specimens with low to moderate sink strength and interpreted as evidence of 1D gliding interstitial clusters. Radiation-enhanced diffusional

☆ This manuscript has been authored by UT-Battelle, LLC under Contract No. DE-AC05-00OR22725 with the U.S. Department of Energy. The United States Government retains and the publisher, by accepting the article for publication, acknowledges that the United States Government retains a non-exclusive, paid-up, irrevocable, worldwide license to publish or reproduce the published form of this manuscript, or allow others to do so. The Department of Energy will provide public access to these results with full access to the published paper of federally sponsored research in accordance with the DOE Public Access Plan (http://energy.gov/downloads/doe-public-access-plan).

* Corresponding author.
E-mail addresses: liny@ornl.gov (Y.-R. Lin), bhattacharya@ornl.gov (A. Bhattacharya), szinkle@utk.edu (S.J. Zinkle).

https://doi.org/10.1016/j.matdes.2023.111668

Vacancy migration energy
Radiation enhanced diffusion
Ion implantation
Safe analysis zone

broadening of implanted Ni ions (at 400–550 °C) in Fe and Fe-Cr was up to 250 nm toward the surface, which leads to a much broader near-peak-damage region where cavity swelling is suppressed. Diffusional broadening of implanted ions is calculated to be similarly pronounced for self-ion irradiations, particularly near the peak and higher swelling temperature regimes. Adequately high ion energies (~8–15 MeV) are recommended for ion-irradiation studies to provide a sufficiently broad midrange safe analysis region with minimized surface and injected ion effects.

1. Introduction

Mobility of point-defects is a fundamental parameter that controls material properties [1] for a wide variety of applications, including fission/fusion nuclear reactors [2–4] and ion-beam processing of semiconductor materials [5,6] and many other materials (e.g., smart materials [7] and nanomaterials [8]). In such applications, the energetic particle bombardment generates an environment where the concentration of point-defects (vacancies and self-interstitial atoms) in a metal or nonmetal is many orders of magnitude higher than for the same material in thermal equilibrium [9]. Depending upon the irradiation temperature, the point-defects then cluster together to form extended defects in the microstructure that are deleterious to material's properties – the study of which is critical to design advanced radiation-tolerant materials.

For fission or fusion energy applications, ion beams have been widely used to study irradiation effects in structural materials, as a surrogate to neutron irradiations. A major advantage of ion irradiations is the ability to rapidly achieve high doses and the irradiation conditions (e.g., temperature and damage rate) can be well controlled, which provides valuable single-variable data for improved understanding of irradiation effects [10]. Compared to neutron irradiation, other advantages of using ion beams include relatively lower cost, shorter irradiation time (higher dose rate), and minimal activation of materials. Although many studies claim that ion irradiation can reproduce the irradiation-induced defects observed in neutron irradiated materials, questions still remain regarding the use of charged ion particles to completely understand neutron irradiation [11–13].

A number of differences in ion and neutron irradiation phenomena have been identified. Several limitations require a cautious experimental design to minimize potential artifacts and a careful data interpretation to warrant relevant comparison with neutron irradiation conditions. Some of the key differences are as follows:

1. Depth profiles of damage level: ion irradiations have a relatively shallow penetration depth with varying dpa (displacements per atom) and damage rate (dpa/s) profile as compared to typical homogeneous dose and dose rate for neutron irradiations.
2. Lack of transmutation products: ion irradiations generally do not induce transmutation reactions, thereby do not produce transmutant gas atoms (e.g. He and H) simultaneously with displacement damage like in neutron-irradiated materials. For ion irradiations, simultaneous multi-ion beam irradiations are typically used to study the He and H synergistic effects [14].
3. Beam pulsing effect: experimental studies [15,16] have shown that the use of a raster-scanned ion beam could suppress void swelling and may also affect evolution of other microstructure features (e.g., loops and precipitate), most likely due to a beam pulsing effect [17]. In general, defocused ion beams are recommended instead of rastered beams to avoid this effect [10,18].
4. Dose rate effect: the dose rate difference between ion (high damage rate typically $\sim 10^{-4}$–10^{-3} dpa/s) and neutron (low damage rates typically $\sim 10^{-9}$ – 10^{-6} dpa/s) irradiations can significantly affect the cavity swelling transient dose [19–21], peak cavity swelling temperature [22–24], loop nucleation [25,26], and ballistic dissolution behavior of secondary phases/precipitates [27,28]. Quantitative temperature shift corrections for different types of defects are often needed to compare irradiations performed at different dose rates [29].
5. Carbon contamination: ion accelerator-induced carbon contamination, which can artificially alter the microstructure (e.g., formation of carbides) and affect the formation of cavities, has been observed in ion irradiated samples [30,31]. The source of carbon uptake could be the residual gas in the accelerator or target chamber. Studies concluded that the incident ion beam may likely crack hydrocarbon components in the residual gas and drag carbon atoms toward the surface [13,32]. Pre-irradiation plasma cleaning and target chamber cold trap techniques are used to minimize carbon contamination [13,33].
6. Stress effect: if irradiation-induced volumetric expansion occurs, the underlying unirradiated substrate produces mechanical constraint in the lateral directions on the ion irradiated layer [34]. Constraint stress may affect the nucleation and growth of loops [35,36]. Additionally, without sufficient gaps between closely arranged samples, compressive stress can be caused due to thermal expansion or cavity swelling [22].
7. Near-surface effect: studies of irradiated materials have reported the existence of loop and cavity defect denuded zones and enhanced swelling regions adjacent to planar point defect sinks (e.g., grain boundaries or free surfaces) in both neutron and ion irradiated materials [35,37–42]. However, in most cases, these observations are limited to a single irradiation condition and the general material-specific dependencies associated with dose, dose rate, and temperature are not evident.
8. Implanted ion effect: injected ions cause chemical effects and imbalance of local point defect concentration (excess of interstitials), which can potentially suppress cavity swelling [43–47], modify the formation of loops [48] and precipitates [49]. On top of this, the diffusional broadening (thermal diffusion plus radiation-enhanced diffusion) of the injected ions can extend the breadth of the implanted ion-affected region [50]. However, experimental data on radiation-enhanced diffusion in model alloy systems are limited.
9. Swift heavy ion effect: the combination of near-surface and implanted ion effects establishes the boundaries of an artifact-free "safe analysis" region near the mid-range of the damage profile [11]. In general, increasing the incident ion energy can provide a larger safe analysis region for microstructure characterization. However, for ultra-high ion energies (typically > 20 MeV, depending on the ion and the material), swift heavy ion effects not associated with elastic collisions have been observed near the ion track, which can lead to enhanced production/annealing of defects and crystalline to amorphous phase transformation [51,52].

In addition, the calculated location of the implanted ion range and corresponding damage profile obtained from computer codes such as SRIM may have possible deviations. A previous study

Table 1
Neutron and ion irradiation conditions. The fast neutron (>0.1 MeV) and Ni ion fluence were ~ 1.1×10^{25} m^{-2} and ~ 9.7×10^{20} m^{-2}, respectively.

Irradiation type	Material	Temperature (°C)	Damage level (dpa)	Damage rate (dpa/s)	He content (appm)	Ref.
Neutron	Cu	182–500	1.1–1.3	~2×10^{-7}	0.2	[54]
	Cu-B				107	[55]
Dual ion	Fe-Cr (0–14 wt% Cr)	400–550	30	~1.4×10^{-3}	3 and 300	[22] and [3]

revealed that SRIM-2013 overestimates the peak position of implanted 8 MeV Ni ions in Fe with a ~ 700 nm shift [22]. Other limitations of ion irradiation studies such as high subthreshold collision energy, high ionization rates, and non-monoenergetic primary knock-on atom energies are summarized by Zinkle and Snead elsewhere [11]. These differences can lead to a higher defect diffusivity and higher surviving defect fraction for ion irradiations.

This work seeks to provide a better understanding of the formation mechanism of the surface and injected ion effects as well as their extended effects on (i) the suppression of cavity swelling and (ii) reduction of safe analysis region for ion irradiation studies. This study examined the cavity (including voids and bubbles, which are under-pressurized cavities and over-pressurized cavities with gas atoms, respectively [53]) denuded zones near free surfaces and grain boundaries from systematic studies, including both published and previously unpublished data of neutron and ion irradiated materials. In addition, the diffusional broadening profiles of implanted ions were examined by Time-of-Flight Secondary Ion Mass Spectrometry (ToF-SIMS) techniques. The result of this study suggests that higher ion energies (>8 MeV) are essential to avoid surface and injected ion effects. In particular for ion irradiation studies, at intermediate temperatures relevant for cavity swelling, the enhanced swelling region adjacent to the cavity denuded zone and diffusional broadening of implanted ions that can potentially shrink the safe analysis region generally cannot be ignored. The fundamental understanding of the near-planar-sink (free surface and grain boundaries) and implanted ion effects on cavity swelling can be applied to many other materials systems. Qualitatively estimation of defect (monovacancy, vacancy cluster, or He-vacancy complexes) migration energies and radiation enhanced diffusivity measured from experimental results may provide valuable inputs for modeling and simulation studies.

2. Experimental methods

The cavity denuded zones near grain boundaries were measured from TEM micrographs of previously examined neutron-irradiated Cu and Cu-B (containing ~ 18 wt ppm ^{10}B) [54,55]. Polycrystalline high purity Cu and Cu-B alloys were irradiated in the B8 site of the Oak Ridge Research (ORR) reactor for a period of 14 weeks using thermocouple-controlled electrical heaters to provide constant irradiation temperatures of 182 to 500 °C. Both materials were irradiated with moderated fission neutrons to a damage level of ~ 1.2 dpa at a damage rate of 2×10^{-7} dpa/s. The fast neutron (>0.1 MeV) fluence was ~ 1.1×10^{25} m^{-2}. For the Cu-B alloy, 107 ± 5 appm He was generated during neutron irradiation from the transmutation reaction with ^{10}B whereas 0.2 appm He was generated in the irradiated pure Cu samples. Further details are provided in refs. [54,55]. A series of dual ion (Ni + He) irradiation experiments performed on Fe-Cr alloys containing 0 to 14 wt% Cr at temperatures 400–550 °C [3,22], which featured well-controlled irradiation temperature with an uncertainty of less than ± 10 °C, were used for the analysis of near-surface and implanted ion effects. The experiments were carried out to a mid-range dose of 30 dpa (damage rate ~ 1.4×10^{-3} dpa/s) with He implantation rates of either 0.1 or 10 appm He/dpa (see Fig. A.1 in the supplemental file for the calculated SRIM dpa and implanted ion distributions). An 8 MeV defocused Ni ion beam with a total fluence of ~ 9.7×10^{20} m^{-2} was selected for its relatively high energy in order to create a sufficiently broad midrange "safe analysis region" as a reference for comparison with near-surface microstructures. The use of Ni as the heavy ion source, distinct from the Fe-rich target specimens, was deliberately chosen to easily quantify the amount of diffusional broadening of the implanted ions during ion irradiation. The He ions implanted simultaneously with Ni ions are used to study the migration behavior (migration energies) for He-vacancy complexes compared to monovacancy behavior. The ion and neutron irradiation conditions are summarized in Table 1. The grain size of the Cu, Fe, and Fe-Cr alloys was approximately 100, 183, and 80–390 μm, respectively.

Two different approaches were used to estimate the near-surface cavity denuded zone width. As illustrated in Fig. 1a, for the average distance method (X_d), a line was drawn parallel to the surface that intersected the cavities located nearest to the free surface or grain boundary, and then the average distance between surface (or grain boundary) to the most nearby cavities was calculated from TEM images. A slope variation method (Fig. 1b) analyzed the depth distribution of the cavity density, and then defined a saturation density located at the transition between the "denuded zone and enhanced swelling region" and the "bulk analysis zone". Ideally, the transition point should be the intercept of a steep and another less-steep best-fit line. The cavity denuded zone width (X_{30} or X_{50}) was then determined using a criterion of either 30% (X_{30}) or 50% (X_{50}) of the saturated cavity density. Both methods have a considerable uncertainty when the cavity density is low and the transition may not be apparent. In addition, for the ion irradiated Fe-Cr samples in this study, He ions were simultaneously implanted in the range of ~ 400–1500 nm. The diffusion of He atoms could strongly affect the vacancy mobility and the formation of cavities. If the denuded zone is near ~ 400 nm, then an additional complication arises due to nonuniform He deposition at depths below and above ~ 400 nm.

The depth profiles of implanted Ni ions in Fe and Fe-10Cr irradiated at 400, 470, and 550 °C were analyzed by time-of-flight secondary ion mass spectrometry (ToF-SIMS) at National Tsing Hua University using a TOF-SIMS 5, manufactured by ION-TOF, Germany. The dual-beam SIMS experimental conditions are summarized in Table 2. Intensities of recorded SIMS depth profiles were converted into atomic concentration scales by considering the total ion dose of 9.68×10^{20} ion/m^2 given by the irradiation experiments. STEM- energy dispersive X-ray spectroscopy (EDS) depth profile of the implanted Ni ions was obtained using an FEI Talos F200X and are shown elsewhere [22].

A set of MATLAB routines were provided by Doyle et al. [50] for radiation-enhanced diffusion (RED) modeling of the depth-dependent dose rate profile, based on Fick's second law and SRIM simulation. The depth dependence of the RED coefficient was modeled following the equation:

$$D_i = D_{max}\left(\frac{G_i}{G_{max}}\right)^E + D_{therm} \quad (1)$$

where D_i and D_{max} are the RED diffusion coefficients of bin i and the maximum damage rate region, respectively, D_{therm} is the thermal diffusion coefficient, E is the exponential scaling factor which is

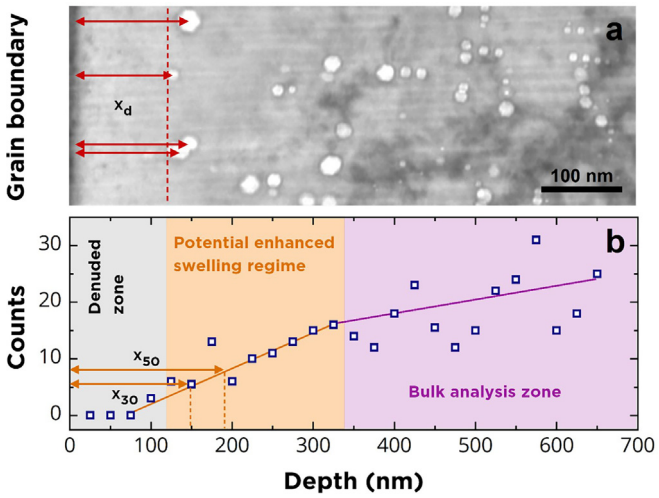

Fig. 1. Example of the (a) average distance method (X_d) and (b) slope variation method (X_{30} and X_{50}) for cavity denuded zone evaluation in dual ion irradiated Fe at 435 °C to 30 dpa (10 appm He/dpa).

Table 2
TOF-SIMS experiment condition.

	Analysis Beam	Sputter Beam
Ion type	Bi	O_2
Energy (KeV)	30	2
Current	1.0 pA	450 nA
Area (μm^2)	100 × 100	260 × 260
Fluence (ions/m^2)	5.8×10^{13}	3.3×10^{19}

set as 0.5 for recombination-dominant conditions, G_i and G_{max} are the damage rates in bin *i* and at the maximum damage rate, respectively. By modifying the correction factor in SRIM, the peak position of the implanted Ni profiles estimated by SRIM was adjusted to overlap with the peak position of Ni profile measured by SIMS (see Fig. A.2. for details). The background level of Ni was set as 0.003 atomic fraction for the model calculation. Note that a background level up to ~ 0.003 Ni atomic fraction may introduce large and undefined errors.

3. Results

3.1. Near-interface effects in neutron-irradiated Cu and Cu-B

3.1.1. Void denuded and enhanced swelling zones in pure Cu

Fig. 2 shows the voids observed in neutron-irradiated Cu at 220 to 350 °C. In the grain interior, the average void diameter and void density were summarized in ref. [54]. The mean void diameter increased with increasing temperature (from 19 to 49 nm at 220 and 350 °C, respectively), while the void density decreased rapidly with increasing temperature (from 1.5×10^{20} to 3.8×10^{19} m^{-3} at 220 and 350 °C, respectively). At 500 °C, voids were not observed in the neutron-irradiated Cu. This study focuses on the void distribution near the grain boundaries (indicated by white arrows in Fig. 2). In Fig. 2, the voids showed spatial homogeneities in size and density, and void denuded zones near grain boundaries were observed for all conditions between 220 and 350 °C. The dependence of the average void denuded zone width (measured by the average distance method described in the experimental section) on irradiation temperature is given in Fig. 3. The void denuded zone width increased steadily from 340 to 750 nm with increasing temperature from 220 to 350 °C, respectively.

Fig. 4 shows the TEM images of cavities near a grain boundary (indicated by dashed white lines) in neutron-irradiated Cu and Cu-B. An enhanced swelling region (indicated by yellow arrows) adjacent to the void denuded zone (indicated by red lines) was observed in the neutron-irradiated Cu at 275–350 °C (Fig. 4b-d). Within the enhanced swelling region, the void sizes are obviously larger than the voids in the grain interior. Fig. 5 illustrates the variation of void density, size, and void swelling as a function of the distance from the grain boundary. At 220 and 250 °C, void density and diameter next to the denuded zone remained relatively stable with increasing distance. However, at 275–350 °C, starting from the boundary of the denuded zone, the density increased and saturated with increasing distance from the nearest grain boundary, while the void size decreased and stabilized. This results in a transition region with enhanced cavity swelling. The extent of the transition region (enhanced swelling region) containing heterogeneously distributed voids is indicated by the horizontal black arrows in Fig. 5. The width of the transition region was approximately doubled at 350 °C compared to 275 °C. In these transition regimes, the void diameters were approximately three times larger than the sizes measured in the saturated region (i.e., grain interior). On the other hand, the void density was roughly four times smaller than saturated values for voids in the transition regions. Because the increase in cavity swelling is roughly proportional to the cube of the cavity size, this results in an enhanced swelling region next to the void denuded zone even with a relatively low density. The void swelling of the enhanced swelling region was up to 6 times larger than the swelling in the grain interior.

3.1.2. Void and bubble denuded zones in neutron irradiated Cu-B

Both voids and bubbles were observed in the neutron-irradiated Cu-B alloys for temperatures between 182 and 400 °C; Fig. 6 shows an example of the cavities occurring next to a grain boundary for the sample irradiated at 350 °C. Tiny cavities (interpreted to be He-filled bubbles) were observed to form within the void denuded zones, which indicates that bubbles have a smaller denuded zone width compared to the void denuded zone next to grain boundaries. As summarized in ref. [55], in the temperature range of 182 to 500 °C, TEM results (in the grain interior) showed that the void diameter increased from 3.2 to 4000 nm, while the void density decreased from 10^{22} to below 10^{14} m^{-3}. At 400 °C, only one void close to the grain boundary was found in the TEM images. In the same temperature range, the mean bubble diameter increased from < 2 nm to ~ 9.5 nm, and the bubble density decreased from 2×10^{21} to 4×10^{20} m^{-3}. Near the grain boundaries, as shown in Fig. 7, similar to the increment of void denuded zones (from 225 to 1784 nm at 182 and 400 °C, respectively), the bubble denuded zone width also increased with increasing temperature (from 32 to 580 nm at 182 and 500 °C, respectively). However, the corresponding denuded zone width for bubbles was 2–6 times smaller than that for voids. Unlike the neutron-irradiated Cu results at 275–350 °C, an enhanced swelling region adjacent to the cavity denuded zone was not found in the neutron-irradiated Cu-B alloys at 182–500 °C. As shown in Fig. 4, an enhanced cavity swelling region (indicated by the yellow arrows) was clearly observed in the neutron-irradiated pure Cu at 350 °C (Fig. 4d), but not in Cu-B at the same irradiation temperature (Fig. 4f).

3.2. Dual ion irradiated Fe and Fe-Cr alloys

3.2.1. Cavity denuded zone

Void denuded zones were also observed in dual ion (8 MeV Ni + 0.1–10 appm He/dpa) irradiated Fe and Fe-Cr (3–14 wt% Cr) alloys at 400–550 °C [3,22,56]. Fig. 8 summarizes the cavity swel-

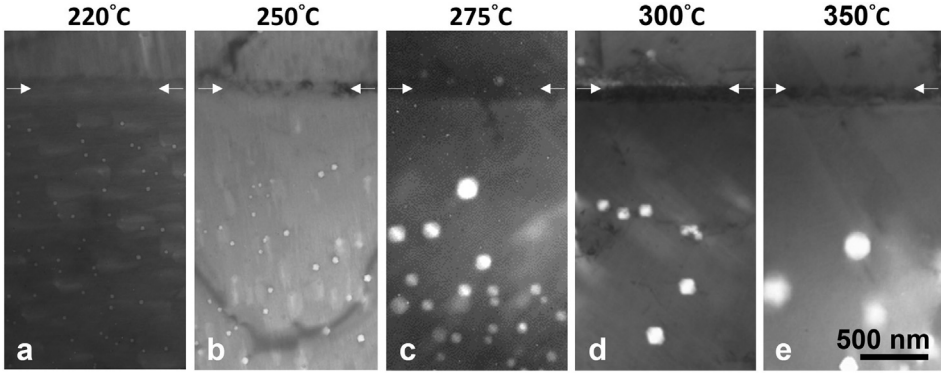

Fig. 2. Grain boundary void denuded zone in neutron-irradiated Cu at (a) 220, (b) 250, (c) 275, (d) 300, and (e) 350 °C to ~ 1.2 dpa. Grain boundaries are indicated by the white arrows.

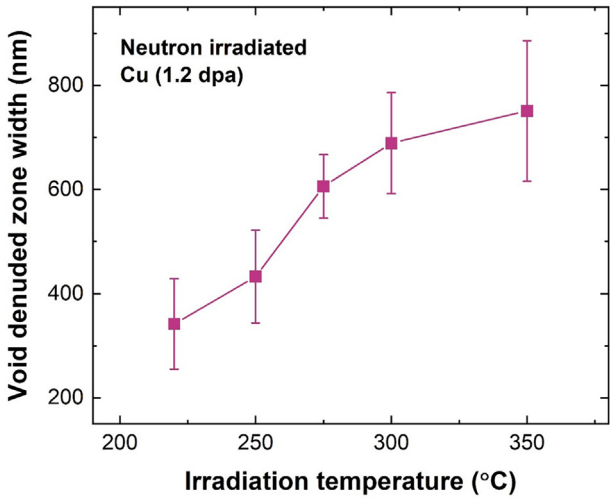

Fig. 3. Void denuded zone width as a function of irradiation temperatures in neutron irradiated Cu to ~ 1.2 dpa.

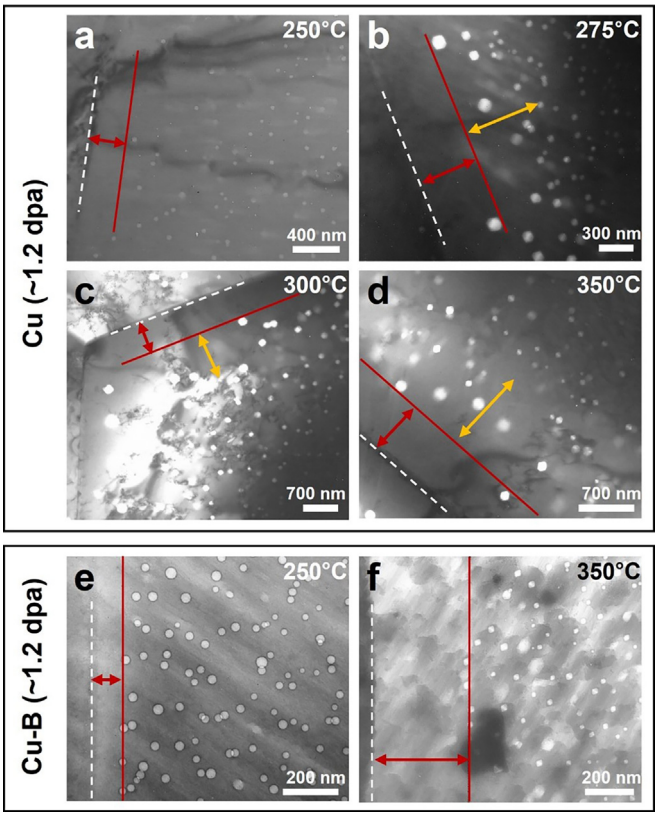

Fig. 4. Distribution of cavities near a grain boundary of neutron-irradiated Cu and Cu-B alloy at 250–350 °C to ~ 1.2 dpa. The calculated He content in the neutron irradiated Cu and Cu-B was 0.2 and 107 appm, respectably. Grain boundaries and void denuded zones are indicated by the dashed white lines and solid red lines, respectively. The red and yellow arrows indicate the cavity denuded zones and enhanced swelling regions, respectively. (For interpretation of the references to colour in this figure legend, the reader is referred to the web version of this article.)

ling of a series of dual-ion irradiated Fe as a function of depth superimposed on the corresponded TEM image. The white dashed lines in the plot mark the area where it is relatively safe to perform an analysis. The red solid line with open squares at the ends signifies the region where helium has been implanted at a constant ratio of He to dpa. The depth-dependent cavity swelling of each condition was calculated with a constant bin width of 250 nm. In Fig. 8, for the irradiation temperature between 400 and 550 °C, both the 0.1 and 10 appm He/dpa irradiated samples typically showed a cavity denuded zone and an adjacent enhanced swelling region near the sample surface (around 0–750 nm). The cavity denuded zone width increased with increasing temperature. At depths above 1500 nm, the swelling was suppressed in all the conditions. Collectively, the suppression of swelling near the surface and the peak of the 8 MeV implanted Ni (~1800 nm) profile was observed in all the examined irradiation conditions. The cavity size and density within the approximate "safe analysis region" (750–1250 nm) of the dual ion irradiated Fe and Fe-Cr materials are reported and discussed elsewhere [3,22,56]. Even with a Ni ion energy up to 8 MeV, Fig. 8 indicates that the safe analysis zone width might be smaller than 750–1250 nm for some conditions, e.g., 0.1 appm He/dpa Fe at 500 and 550 °C.

The cavity distribution of the Fe-10Cr alloy irradiated at 470 °C and 10 appm He/dpa was selected for detailed examination (Fig. 9). A cavity denuded zone and an adjacent enhanced swelling region were observed not only near the sample surface but also near grain boundaries. The near-surface cavity denuded zone width (~250 nm) extends to a roughly fixed distance into the material, while the cavity denuded width near the grain boundary gradually decreases with increasing depth (increasing dose rate), dropping to near-zero at a depth of ~ 2 μm (Fig. 9b). Since both the accumulated dose and dose rate of ion irradiation studies depend on the depth, the variation of cavity denuded zone width as a function of depth in Fig. 9b indicates the potential impact of dose or dose rate on cavity denuded width. According to existing void nucleation models [23,29,57], the dose rate (vacancy supersaturation

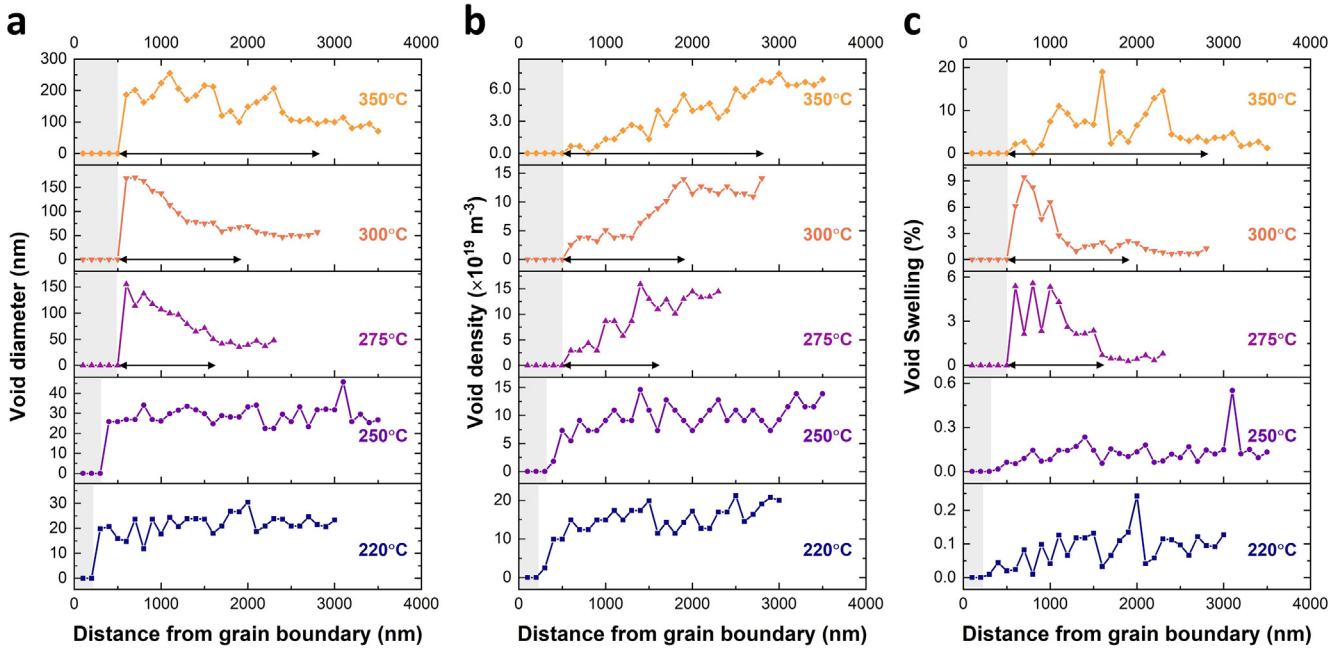

Fig. 5. Variation of void (a) size, (b) density and, (c) swelling with the distance from grain boundary in neutron-irradiated Cu. The cavity denuded zones are marked by the gray area, and the transition regions (enhanced swelling regions) are indicated by the black horizontal arrows.

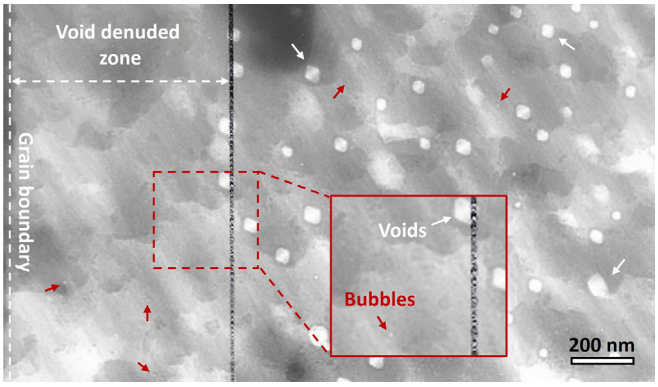

Fig. 6. Voids and bubbles in neutron irradiate Cu-B alloy at 350 °C to ~ 1.2 dpa and ~ 107 appm He. Several voids and bubbles are indicated by the white and red arrows, respectively. (For interpretation of the references to colour in this figure legend, the reader is referred to the web version of this article.)

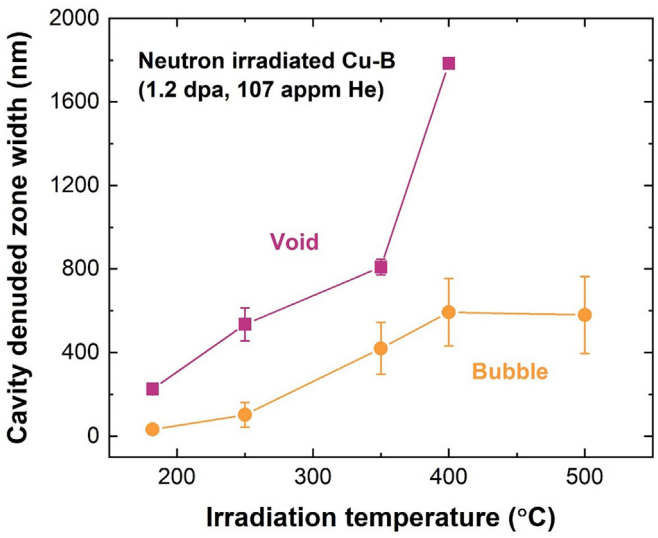

Fig. 7. Cavity denuded zone width of neutron-irradiated Cu-B alloy at 182–500 °C. The denuded zone width of voids (purple squares) and bubbles (yellow circles) was measured separately. (For interpretation of the references to colour in this figure legend, the reader is referred to the web version of this article.)

value) exerts the predominant effect on cavity formation. For recombination dominant conditions, increasing the dose (or displacement damage) rates theoretically reduces the cavity denuded zone width [58]. Besides, in Fig. 9b, the grain boundary cavity denuded zone width near the surface is up to 2.5 times as large as the surface denuded zone width (dashed line). This is most likely due to the combined effects of surface and grain boundary sinks. In the inset image of Fig. 9a, small bubbles were observed within the void denuded zones, indicating that bubbles have a smaller denuded zone width compared to voids. This is consistent with the void and bubble denuded zones observed in neutron irradiated Cu-B (Fig. 6), with transmutant He gas atoms.

3.2.2. SIMS study on implanted Ni ions

Diffusion broadening of the implanted ions is of concern because these injected interstitial atoms can suppress cavity swelling [43,59,60]. However, if typical "self-ion" irradiations (Fe ions in this case) would be performed, it would be difficult to monitor the diffusional broadening of the implanted ions unless special techniques were used such as implantation of special isotopes. Therefore, Ni ions were used for the bombarding (implanted) ion species since it is easy to follow the diffusional broadening of ions that are not part of the target material composition. A molecular dynamics study by Shu and Chongyu [61] reported that the migration energy of self-diffusion in Fe was 15–30% (depending on the diffusion orientation) lower than the migration energy of nickel diffusion in Fe. This indicates that diffusional broadening could be even more significant in self-ion irradiated Fe, compared to Ni ion irradiated Fe. Fig. 10 shows the profiles of implanted 8 MeV Ni ions in Fe and Fe-10Cr irradiated at 400, 470, and 550 °C as analyzed by SIMS. Further analyses of the thermal diffusion and radi-

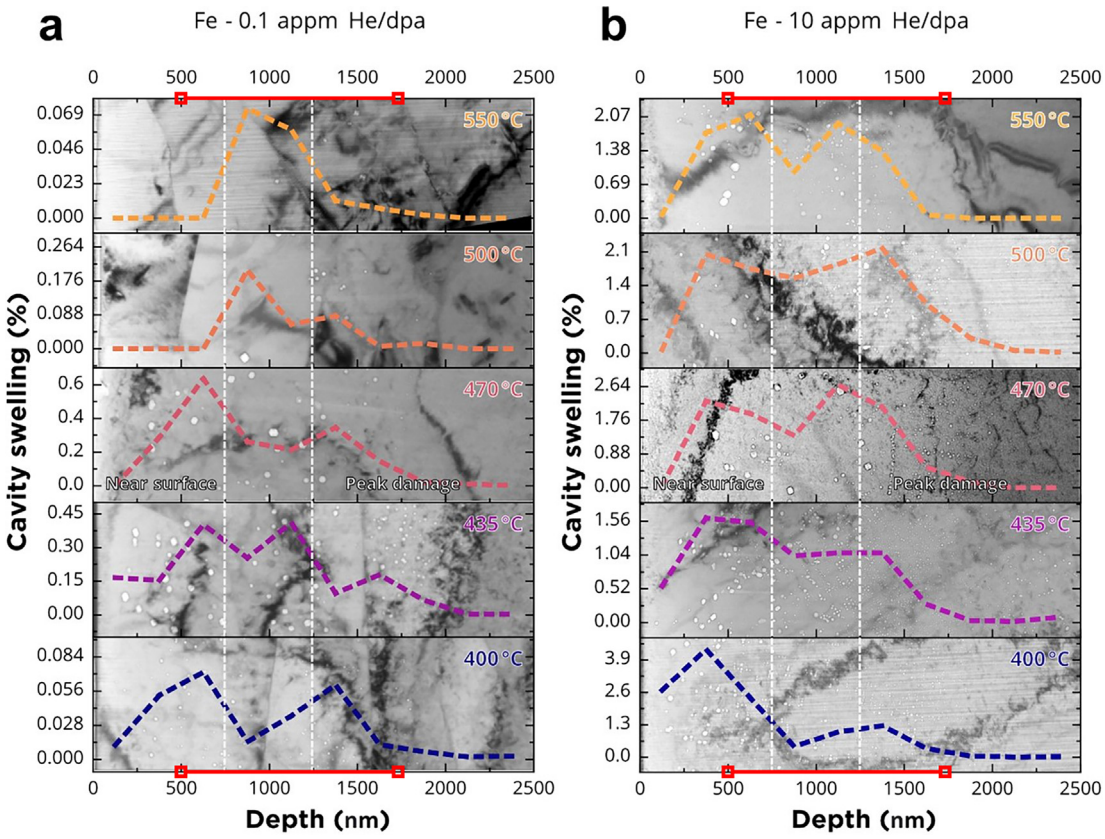

Fig. 8. Comparison of the depth distribution of cavity swelling in Fe irradiated up to ~ 30 dpa at 400–550 °C with (a) 0.1 and (b) 10 appm He/dpa. The quantitative cavity swelling vs. depth is denoted by the dashed colored lines. The white dashed vertical lines mark the area where it is relatively safe to perform an analysis. The horizontal red solid lines with open squares at the ends signify the region where helium has been implanted at a constant ratio of He to dpa. (For interpretation of the references to colour in this figure legend, the reader is referred to the web version of this article.)

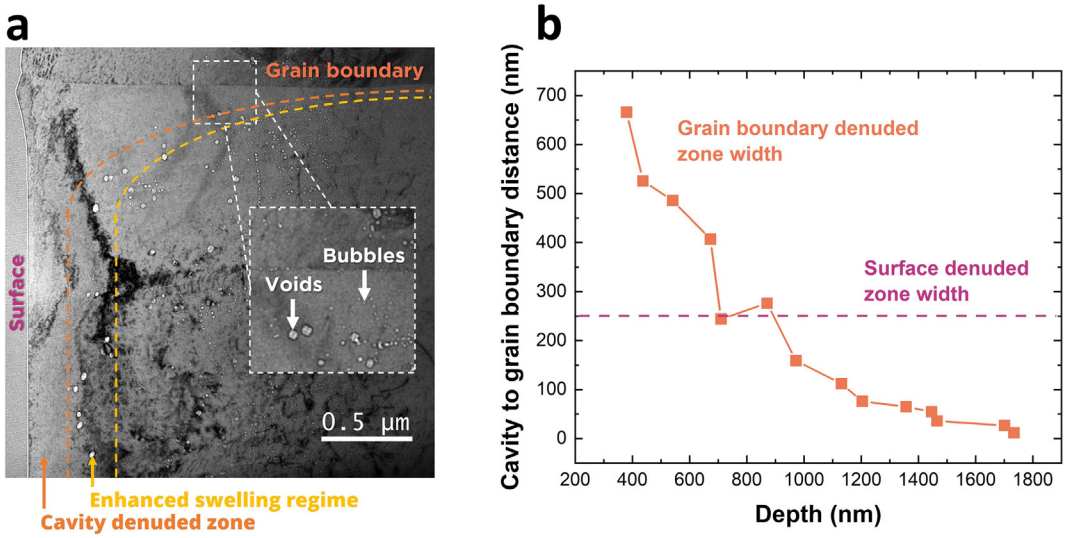

Fig. 9. (a) TEM image of a dual ion irradiated Fe-10Cr at 470 °C showing the cavity denuded zone width and enhanced swelling region (b) Corresponding depth-dependent cavity denuded zone width near the grain boundary and sample surface.

ation enhanced diffusion (RED) broadening of the implanted ion profiles were conducted by fitting model-generated (Eq. (1)) [50] ion profiles to relevant experimental profiles obtained from SIMS (Fig. 10). Pronounced diffusional broadening (decrease in peak implanted Ni concentration and increased full width half maximum of the SIMS-measured implanted Ni distribution) compared to SRIM calculation is evident in Fig. 10a. With a fixed D_{therm} for 550 °C (cf. Eq. (1) in section 2), the model-generated profiles showed the best fit to the SIMS profile with D_{max} of 5×10^{-18} m^2/s (Fig. 10a). The temperature variation from 400 to 550 °C shows an insignificant effect on the thermal diffusion broadening of the implanted ion profiles (Fig. 10b). The listed D_{therm} values of

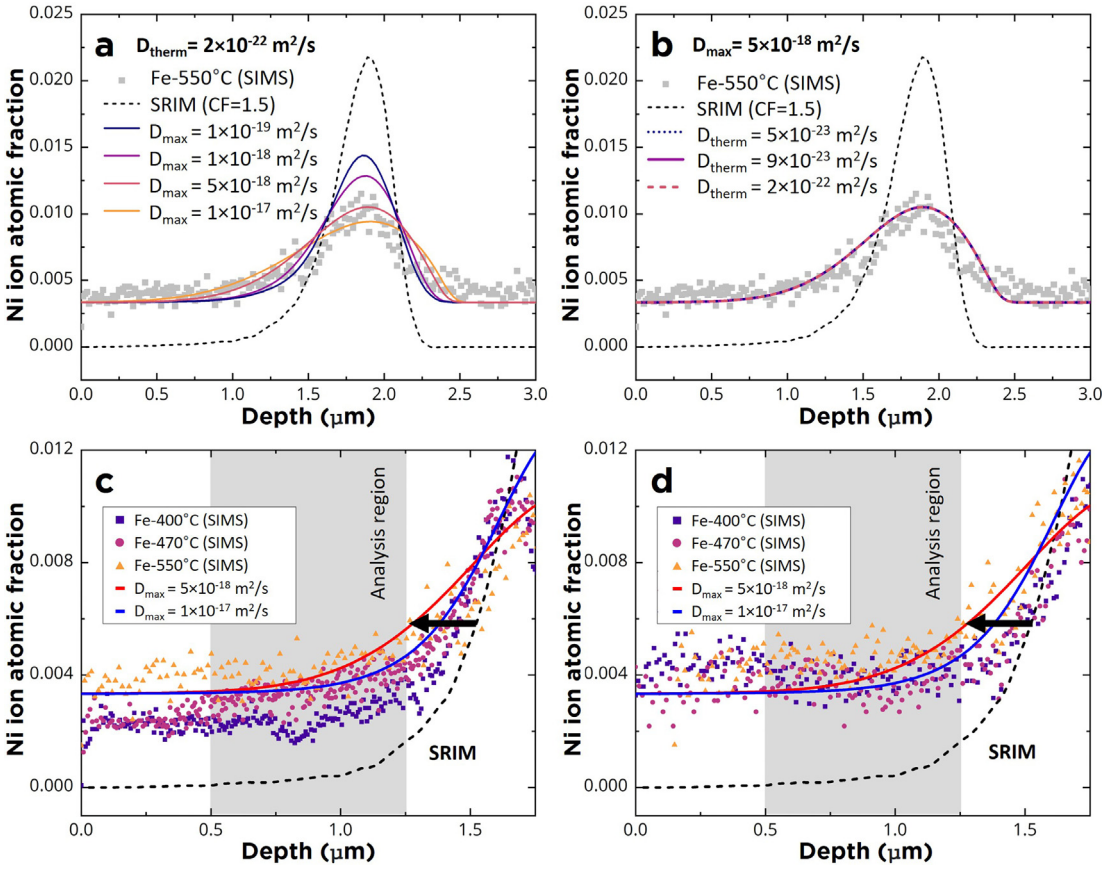

Fig. 10. Implanted 8 MeV Ni profile from model predictions and SIMS measurement. (a) demonstration of the peak diffusion coefficient effect, (b) demonstration of the of temperature effect, (c-d) Implanted Ni profiles in Fe and Fe-10Cr near the TEM analysis regime. CF is the correction factor in SRIM.

5×10^{-23}, 9×10^{-23}, and 2×10^{-22} m^2/s correspond to the reported Ni atom thermal diffusivity in Fe at 400, 470, and 550 °C [62,63]. Comparison of the injected Ni ion profile near the TEM analysis regime for Fe and Fe-10 are shown in Fig. 10c and d, respectively. For pure metals, the radiation-enhanced diffusion (RED) coefficient is defined as [33]:

$$D_{rad} = D_v C_v + D_i C_i \tag{2}$$

where $D_{i,v}$ is the point defect diffusivity and $C_{i,v}$ is the point defect concentration (i and v refer to interstitials and vacancies). With a high dose rate of ion irradiation, the elevated vacancy and interstitial concentrations can boost the radiation-enhanced diffusion coefficient to values that are orders of magnitude larger than the thermal diffusion coefficient, as observed for the fitted D_{max} (5×10^{-18} m^2/s) and D_{therm} ($\sim 2 \times 10^{-22}$ m^2/s) values for Fe-10Cr irradiated at 550 °C (Fig. 10). The pronounced RED and the co-effect of thermal diffusion (Eq. (1)) can result in a considerable broadening of injected ion profiles, drastically different from the original SRIM predictions. As shown in Fig. 10c and d (indicated by the black horizontal arrows), the combined radiation and thermal broadening of the implanted ion profile could shift the implanted ion-affected regime up to ~ 250 nm toward the surface at 550 °C. In Fig. 10c and d, a critical implanted ion concentration of 0.6 at% (~0.01 at %/dpa near the peak damage zone) was assumed to induce significant suppression of cavity nucleation and swelling, based on prior modeling studies [48,59,60].

4. Discussion

4.1. Estimation of vacancy and vacancy-He defect migration energies from cavity denuded zones

The presence of cavity denuded zones at grain boundaries has been observed in numerous electron, ion and neutron irradiated materials [40,64–69]. The origin of these zones is considered to be connected with the sink strength of grain boundaries or free surfaces, which act as strong neutral sink sites for point defects [70]. The flow of point defects toward the grain boundary reduces the vacancy supersaturation below the critical value needed for void nucleation. In the framework of rate theory, the planar sink (free surface or grain boundary) denuded zone width can be expressed in two limiting cases [71–73]:

1. Sink dominant

$$L \propto \sqrt{\frac{1}{C_s}} \tag{3}$$

2. Recombination dominant

$$L \propto \left(\frac{D_i D_v}{\alpha G}\right)^{\frac{1}{4}} \tag{4}$$

where L is the denuded zone width, C_s is the sink concentration, $D_{i,v}$ are the diffusion coefficients of interstitials and vacancies, $\alpha = 4\pi r_0(D_i + D_v) \sim 4\pi r_0 D_i$ is the vacancy-interstitial recombination coefficient, r_0 is the spontaneous recombination radius, G is the dose rate, and

$$D_v = D_0 e^{\frac{-E_m}{kT}} \tag{5}$$

where D_0 is the diffusion coefficient, E_m is the migration energy, k is the Boltzmann constant, and T is the irradiation temperature. When the density of dislocation loops or cavities (or other defect sinks such as precipitates) is relatively high, the denuded zone width would be expected to follow the sink-dominant relationship (Eq (3)). On the other hand, a recombination-dominant condition with relatively low defect densities would follow Eq (4).

For the recombination dominant case, since$\alpha \sim 4\pi r_0 D_i$, Eq (4) becomes $L \propto (D_v/G)^{1/4}$. Therefore, substituting Eq (5) into Eq (4), the void denuded zone width (L) would be proportional to $exp(\frac{-E_m}{4KT})$. Consequently, the vacancy migration energy can be estimated from the slope of an Arrhenius plot (ln(L) vs. 1/kT) multiplied by a factor of 4. For cases where sink-dominant kinetics occur (e.g., high precipitate densities or irradiation near the lower limit for void swelling where a high density of dislocation loops may co-evolve), then the vacancy migration energy cannot be extracted from an analysis of the temperature dependence of the cavity denuded zone near planar sinks. The radiation-induced sink density typically decreases with increasing temperature, but the temperature dependence of this variation in sink density is controlled by interstitial loop coarsening, stacking fault tetrahedra thermal dissociation, or other phenomena, and is not simply related to vacancy migration processes. Therefore, a complex temperature dependence (not simply related to the vacancy migration energy) typically occurs for sink-dominant irradiation conditions.

4.1.1. Neutron irradiated Cu and Cu-B

Fig. 11 summarizes the measured cavity-denuded zone widths as a function of inverse temperature for neutron and ion irradiated Cu and Cu-B alloys as measured in the present study and several prior publications. The denuded zone widths were normalized to the same displacement damage rate at 2×10^{-7} dpa/s following Eq (4). Besides statistical error, variability of the average denuded width at the same temperature may also be due to the grain orientation or misorientation of specific grain boundaries [74]. Fig. 11 shows that the normalized void denuded zone width of neutron and self-ion irradiated Cu (including the Cu-B alloy) were distributed near the same fitted line. The slope of this line gives E_m = 0.72 eV, which agrees with the experimental data and the theoretical value for the vacancy migration energy in Cu of 0.70–0.72 eV) [62,75,76]. The voids in the 1 dpa neutron irradiated Cu specimens contained on average ~ 100 to 400 He atoms, with a corresponding relatively dilute He/vacancy ratio of ~ 0.001.

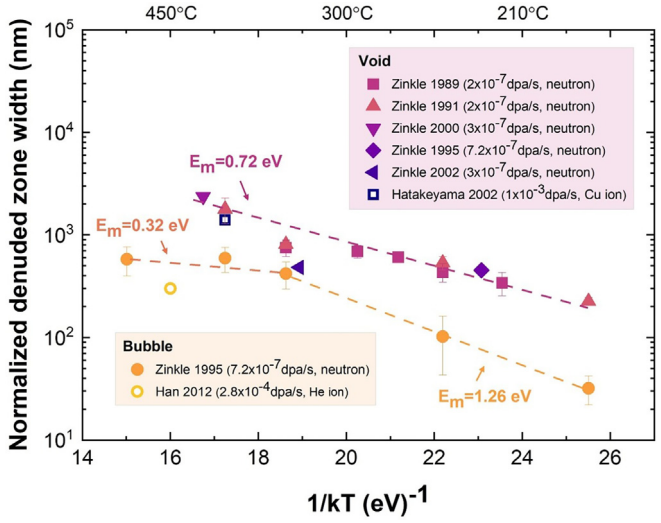

Fig. 11. Cavity (void and bubble) denuded zone width at grain boundaries or surfaces as a function of inverse temperature of neutron and ion irradiated Cu. [25,54,55,74,77–79]. The E_m values in this plot assume recombination-dominant conditions, $L \propto (D_v/G)^{1/4}$.

With the addition of ~ 500X higher concentration of He atoms in the neutron-irradiated Cu-B alloy, the bubble denuded zones were closer to the grain boundary compared to the void denuded zone (Figs. 6 and 7). This result is consistent with the single He ion implantation study by Han et al. [74], which also showed a relatively small dose rate-normalized bubble denuded zone width (~200 nm) at 450 °C, as shown in Fig. 11. In the same figure, the bubble denuded zone width data were fitted by two yellow-dashed lines with an apparent slope change at ~ 350 °C. The fitted "effective" migration energy value below 350 °C was 1.26 eV, whereas above 350 °C the apparent activation energy for vacancy migration was reduced to 0.32 eV. Prior studies have generally found that He additions cause an increase in the migration energy of He-vacancy clusters compared to the Cu monovacancy migration energy [80–82]. Density functional theory (DFT) calculations indicated that multiple migration pathways exist for He-vacancy complexes depending on the He/vacancy ratio. According to the simulation results from Gonzalez et al. [80] and Dunn et al. [81], at lower temperatures (<350 °C), the He-vacancy complexes of HeV_3 (E_m = 1.14/0.84 eV), HeV_2 (E_m = 0.93/0.86 eV) or HeV + V (E_m = 0.96 eV) would be the possible candidates dominating the formation of the bubble denuded zone width. Ref [80] calculated He-vacancy complex migration energies for a two-step process and direct exchange migration that ranged from 0.90 to 2.5 eV. The upper limit for He-vacancy complex migration energy may be attributable to He-vacancy dissociation; an experimental estimate of ~ 2.0 eV was measured by thermal desorption experiments in He-implanted Cu [82]. A table of the migration energy of different point defect clusters in Cu is summarized in Table. A.1. The apparent decrease in the activation energy above 350 °C in Fig. 11 might be attributable to thermal-activated dissociation of small He-vacancy complexes at these high temperatures, which would cause other diffusion mechanisms to control the kinetics of the bubble denuded zone at high temperatures. Further work is needed to investigate this possibility.

4.1.2. Neutron and ion irradiated Ni

Fig. 12 summarizes several published temperature-and dose rate-dependent observations of void denuded zones adjacent to grain boundaries in ion and neutron irradiated Ni [66,83–85]. The activation energy obtained from the slope of the Arrhenius plots in Fig. 12 is close to 0.36 eV for all four data sets, which corresponds to a vacancy migration energy of ~ 1.44 eV if recombination-dominant conditions are valid (Eq. (4)). The reported values for the vacancy migration energy in nickel range from 1.04 to 1.5 eV from modeling and experimental studies [62,75,86–88]. The denuded zone results are therefore consistent with the upper range of these prior experimental and modeling estimates of Ni vacancy migration energy.

Similarly, from our reanalysis of the void surface-denuded zone results in 1 MeV electron irradiated types 316L, 316 and 304 austenitic stainless steel reported by Garner and Thomas [89], the activation energy at irradiation temperatures of 460 to 550 °C is 0.35 eV, which corresponds to a vacancy migration energy of 1.4 eV in these steels (same as obtained for pure Ni in Fig. 12) assuming recombination-dominant irradiation conditions. A higher activation energy of 0.69 eV was observed in the surface-denuded void data for electron irradiation temperatures above 550 °C. The physical meaning of this higher activation energy at high temperatures is uncertain. Garner and Thomas [89] suggested that the elevated activation energy above 550 °C, which is half the vacancy migration energy in these steels, may be associated with γ-iron.

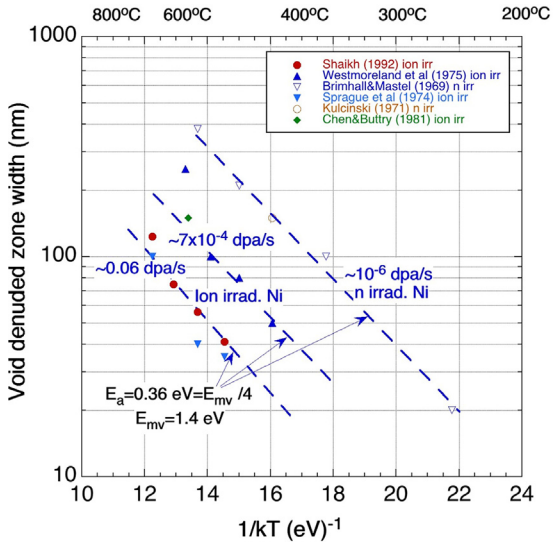

Fig. 12. Cavity (void) denuded zone width at grain boundaries or surfaces as a function of inverse temperature for neutron and ion irradiated Ni. Ref. [42,66,83–85,92]

We are not aware of prior studies of cavity denuded zones in irradiated Ni containing significant (≫1 appm) He concentrations, so we cannot assess the migration energies of He-vacancy complexes from cavity denuded zone studies. Prior experimental He implantation and modeling studies reported rate-controlling migration energies of 1.9–2.6 eV for He-vacancy complexes in Ni [82,90,91]. Consistent with the reported results for Cu discussed in section 4.1.1, the effective migration energy for He-vacancy complexes is significantly higher than for monovacancies.

4.1.3. Dual-ion irradiated Fe and Fe-Cr

Although the inset near-grain boundary image in Fig. 9 may evince that the dual ion-irradiated Fe and Fe-Cr samples also have separated bubble denuded zones like in neutron irradiated Cu-B (Figs. 6 and 7), the bubble density near the free surface in most of the ion irradiated Fe and Fe-Cr alloys was relatively low and a clear bubble denuded zone width could not be accurately measured. Therefore, only void denuded zone widths were measured for the dual ion irradiated samples. Based on the bimodal size distribution of cavities in the irradiated Fe-Cr alloys, cavities with radius below and above 2 nm were classified as bubbles and voids, respectively. Fig. 13 collects the void denuded zone width measurements obtained from the surface region of ion-irradiated Fe and Fe-Cr alloys with 0.1 appm He/dpa [22] and 10 appm He/dpa [3,56] from our previous studies. In Fig. 13, the void denuded zone widths were measured using two methods: the averaged distance X_d (represented by solid lines) and slope variation $X_{3,5}$ (represented by shaded areas). The $X_{3,5}$ method estimates the denuded zone width from the saturated cavity density using a criterion of 30% or 50% of the saturated cavity density. The measured void denuded zone width of all the irradiated Fe and Fe-Cr samples is plotted as a function of inverse temperature in Fig. 13. Overall, the void denuded zone width increased with increasing temperature. Below 435 °C, the denuded zone width of the Fe-Cr alloys is 2–4 times smaller than in Fe. The denuded zone width differences reduce to below a factor of two at higher temperatures. For the Fe denuded zone width, as shown in Fig. 13a, the three lower temperature data points (400–470 °C) of the 0.1 appm He/dpa irradiations agree well with the 10 appm He/dpa irradiated samples. However, deviations of the denuded zone width between the 0.1 and 10 appm He/dpa irradiated samples are observed at temperatures above 500 °C in Fe-10Cr (Fig. 13c) and Fe-14Cr (Fig. 13d).

As shown in Table 3, following Eq (4) for recombination dominant conditions, the calculated denuded zone widths were applied to estimate the vacancy migration energy, and the estimation indicates that the vacancy migration energies of Fe-3Cr, Fe-10Cr and Fe-14Cr are 2–3 times larger than Fe. This conflicts with previous DFT studies [93] which predict lower vacancy migration energies for Fe-Cr alloys (with 3–14% Cr) than Fe by a factor of 0.7. Unlike the vacancy migration energy estimated from neutron irradiated Cu results (Fig. 11), the vacancy migration energies of Fe (0.96–1.14 eV) estimated from cavity denuded zone widths in the dual ion irradiated samples are not consistent with typical reported values for pure Fe (~0.55–0.71 eV) [62,75,94]. The higher migration energies observed in the dual-ion (with co-injected He ions) irradiated Fe and Fe-Cr alloys may indicate the formation of He-vacancy complexes, which may have higher migration energies than monovacancies. Simulation studies by Gao et al. [95] and Fu et al. [96] reported the migration energy for a HeV_2 in Fe of 1.13 and 1.1 eV, respectively. This calculated increase in migration energy for He-vacancy clusters compared to monovacancies in Fe agrees with the Cu-B results (Fig. 11) and infers that the diffusion of implanted helium atoms or the formation of He-V complexes near the surface in the dual-beam irradiated Fe and Fe-Cr alloys may increase the effective vacancy migration energy.

From another point of view, the irradiation condition could be closer to a sink dominant condition rather than a recombination dominant condition. In Eq. (3), for a sink dominant condition the value of C_s will depend on dose rate (square root dependence for electron irradiation conditions) and temperature (due to point defect binding energy effects and other temperature-dependent processes). In general, the slope of the temperature-dependent denuded zone width for sink dominant conditions cannot be simply related to vacancy migration energies. To evaluate if a recombination dominated condition is operational, the η parameter (Eq. (6)), derived from the rate theory [57], can be used [97,98]. When $\eta \ll 1$, recombination is negligible and the system would be close to a sink-dominant condition.

$$\eta = \frac{4G\alpha}{(K_{is}^2 D_i)(K_{vs}^2 D_v)} \approx \frac{4\pi G r_0}{K_{is}^2 K_{vs}^2 D_v} \tag{6}$$

where K_{is}^2 and K_{vs}^2 are the total sink strengths for interstitial and vacancy absorption into sinks, and D_v is given by Eq (5). For the ion irradiated Fe and Fe-Cr materials in this study, the following equations were used to estimate K_{is}^2 and K_{vs}^2.

$$K_{is}^2 = S_D + S_C \approx K_{vs}^2 \tag{7}$$

where the sink strength of dislocations (S_D) and cavities (S_C) are estimated by

$$S_D = Z_D \rho_D \tag{8}$$

and

$$S_C = 4\pi r N (1 + S_{tot}^{0.5} r) Z_C \tag{9}$$

where $Z_{D,C}$ is the capture efficiency of dislocations and cavities ($Z = 1$ for unbiased sink), ρ_D is the dislocation density, r is the radius of the cavities, N is the cavity number density, and we assumed that the total sink strength S_{tot} is dominated by S_C.

The calculated η values of dual ion irradiated Fe at 400–550 °C with 10 appm He/dpa are plotted in Fig. 14. The defect densities and sizes for the sink strength calculations were extracted from Ref. [3]. As shown in Fig. 14, although the η values before irradiation and at low irradiation temperatures (400–435 °C) are above one, the η values decrease to $\sim 5 \times 10^{-2}$ at higher irradiation temperatures (470–550 °C). This indicates that the system may be

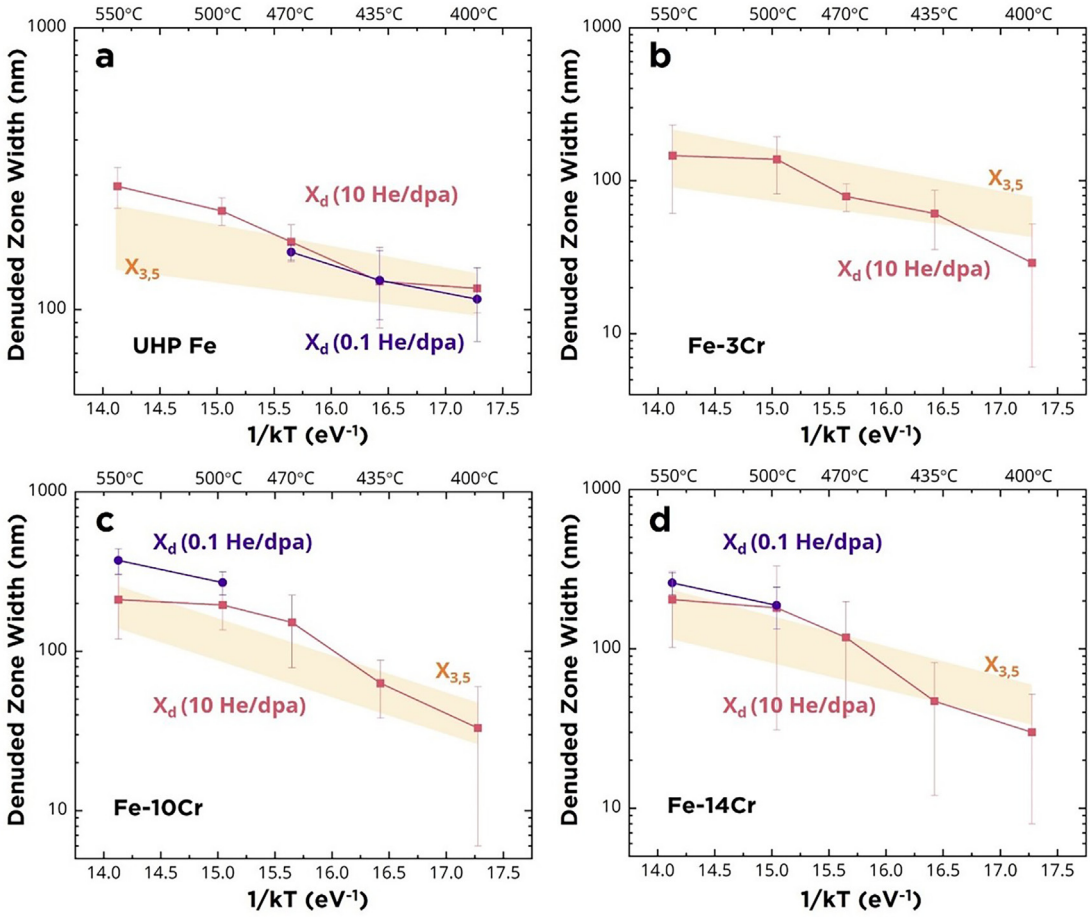

Fig. 13. Void denuded zone width as a function of the inverse temperature of dual ion irradiated (a) Fe, (b) Fe-3Cr, (c) Fe-10Cr, and (d) Fe-14Cr. X_d stands for the average distance method. $X_{3,5}$ denuded zone width estimated from the saturated cavity density is depicted as the shaded yellow band in the plots. The lower extent refers to X_{30} and the upper extent refers to X_{50}. (For interpretation of the references to colour in this figure legend, the reader is referred to the web version of this article.)

Table 3
Estimated vacancy migration energy of dual-ion irradiated Fe and Fe-Cr alloys. The values were estimated using the averaged distance method (X_d) and the average of $X_{3,5}$ using the slope variation method. Experimental method shows large variation in the measured values.

Material	Vacancy migration energy, E_m (eV)			
	10 appm He/dpa X_d	10 appm He/dpa $X_{3,5}$	0.1 appm He/dpa X_d	DFT Costa (2014) [93]
Fe	1.14 ± 0.53	0.44 ± 0.23	0.96 ± 0.33	0.71
Fe-3Cr	2.01 ± 1.15	0.97 ± 0.49	–	0.52
Fe-10Cr	2.32 ± 1.24	1.27 ± 0.53	1.22 ± 0.61	0.43
Fe-14Cr	2.36 ± 1.41	0.91 ± 0.46	1.31 ± 0.82	0.51

evolving from the recombination dominant ($\eta \gg 1$) to sink dominant conditions ($\eta \ll 1$) during irradiation at higher temperatures. Thus, for dual ion irradiation at 470–550 °C the system may be operating in the sink dominant condition, and Eq (4) could then not be used for vacancy migration energy estimation. Note that at a given temperature, the D_v and sink strength values will be lower at low dose rates (e.g., neutron) compared to high dose rates (e.g., ion) [98]. In this case, the η ratio will only decrease by a moderate amount for typical neutron irradiation dose rate conditions compared to ion irradiations. Therefore, for neutron irradiation studies, the value of η obtained in this study may not be valid for evaluating recombination or sink dominated conditions.

In Fig. 13, when selecting the lower and higher three temperatures for slope fitting, the calculated vacancy migration energies were significantly different. This could be due to a transition from recombination dominant to sink dominant condition, or an artifact from the enhanced diffusional broadening of implanted ions at higher temperatures. The latter effect will be discussed in section 4.3. In any case, large uncertainties (up to 50%) exist in the vacancy migration energies. The cavity denuded zone width method works well for some materials such as Cu or Ni, but may have problems in alloys (especially if precipitates may form during the irradiation). The potential high sink strength effect associated with precipitation during irradiation (e.g., α' precipitation in Fe-Cr alloys containing > 9%Cr)) could suppress cavity swelling and affect the estimation of vacancy migration energy. Nevertheless, the cavity denuded zone width method represents a useful experimental approach to obtain qualitative trends when comparing different alloys. Disadvantages of this approach are the requirement of a relatively high number density of cavities and the relatively large

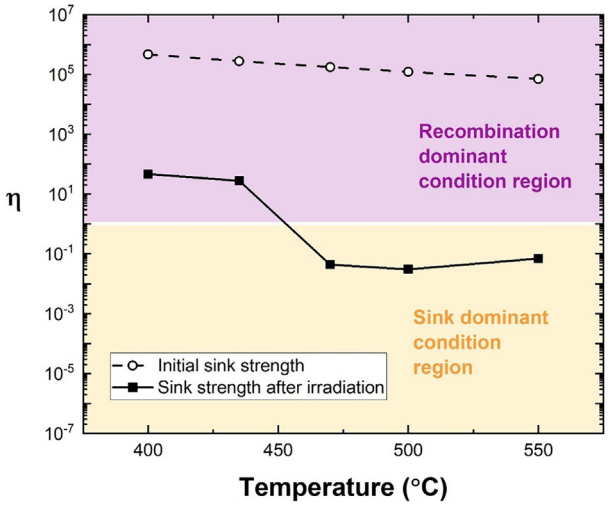

Fig. 14. Calculated η values versus irradiation temperature for dual-ion irradiated Fe with 10 appm He/dpa. A value of $\eta \ll 1$ indicates operation in a sink-dominated condition, whereas $\eta \gg 1$ indicates operation in a recombination-dominated condition.

number of experimental data points needed to minimize statistical errors. This experimental method for estimating vacancy migration energy is best suited for studying materials with poor to moderate swelling resistance where experimental uncertainties in cavity size/density measurements can be minimized. Materials with exceptional cavity swelling resistance are obviously not amenable for this method.

4.2. Enhanced swelling region adjacent to void denuded zone

An enhanced cavity swelling adjacent to the cavity denuded zone along grain boundaries (Figs. 5 and 8) has been experimentally observed in numerous irradiated materials (e.g., Al, Ni, Cu, Fe, V, and Nb) [37,71,99–102]. The transition regime is also referred to as a localized peak swelling or enhanced swelling region. However, such an enhanced swelling region was also not observed in many other irradiated materials with different irradiation conditions [103–105]. Trinkaus et al. [37] proposed a model for this phenomenon in terms of 1D and 2D self-interstitial atom (SIA) transport to estimate the cavity swelling versus distance from a grain boundary. This model suggested that enhanced swelling rate is related to displacement dose and cavity spacing. According to molecular dynamics (MD) simulation studies, 1D-SIA migration in BCC-Fe is more energetically favorable compared to 2D migration [106,107]. In-situ TEM experimental studies have also observed 1D motion of SIA in BCC-Fe [108], but not 2D migration. Based on these reports, it is suspected that the formation of the enhanced swelling region may be mainly related to 1D-SIA migration. In the present study, enhanced swelling regions (Figs. 4 and 5) were observed in neutron-irradiated Cu at intermediate temperatures (275, 300, and 350 °C). For these three irradiation temperatures, the enhanced swelling peak occurs at ~ 10 λ from the grain boundaries, where λ is the average cavity spacing. An enhanced swelling region was not found in any of the neutron-irradiated Cu-B samples irradiated at 182 to 500 °C.

Because of the microstructural evolution of defects at elevated temperatures, localized peak swelling phenomenon might be correlated with sink strength of the irradiation-induced defects, such as dislocation loops, voids, or stacking fault tetrahedra (SFT). Assuming that cavities and SFTs are all spherical defects and using Eq (9), the calculated sink strength of cavities and loops in Cu and Cu-B at 250–350 °C are summarized in Table 4. The sink strength of loops was assumed to be πdN, where d and N is the loop diameter and loop number density, respectively. The sink strength calculations were based on bulk (middle of grain) defect measurements. The density and size of the defects for the sink strength calculations were taken from Refs. [54,55]. In Table 4, for the specimens without visible peak swelling zones (Cu at 250 °C, and Cu-B alloy at 250 and 350 °C), the sink strengths were near or above ~ 10^{14} m^{-2}. As for Cu irradiated at 275, 300, and 350 °C, where the enhanced swelling regions were present, the sink strengths were on the order of 10^{13} m^{-2}. This suggests that when the total sink strength is near or above ~ 10^{14} m^{-2}, 1D gliding of SIAs may be suppressed by the high sink strength. Conversely, when the total sink strength is below ~ 10^{14} m^{-2}, interstitial clusters may exhibit preferential 1D glide from the grain interior to the free surface or grain boundary, and leave an enhanced swelling zone next to the void denuded zone. This is in accordance with the recent study by Wang et al. [109] on irradiated Cu alloys where a similar suppression of 1D gliding defect clusters (loss of precipitate coherency beyond the ion damage zone) was observed when the precipitate sink strength approached or exceeded ~ 10^{14} m^{-2}.

As for the dual ion irradiated Fe (Fig. 8), the enhanced swelling region next to the surface denuded zone is observed in nine out of the ten irradiation conditions at 400–550 °C. The only exception is the 0.1 appm He/dpa irradiated Fe sample at the highest irradiation temperature of 550 °C, even though it had a relatively low calculated cavity sink strength of 2.2 × 10^{-13} m^{-2}. This could be due to the effect of sub-grains near the surface (caused by the strain associated with thermal expansion for samples arranged closely without gaps) or simply because of the statistical error of low cavity density in high-temperature irradiated samples. The increased diffusivity of the implanted He and Ni ions at higher temperatures could also have potential effects. In addition, the width of the region of enhanced swelling (<500 nm) is smaller than in the neutron irradiated Cu (>1000 nm), as shown in Fig. 5. This supports the model predicted by Trinkaus et al. [110], where the width of enhanced swelling region in fast fission neutron irradiated metals is significantly larger than those irradiated by 600 MeV protons. They suggested that when the He production rate is sufficiently high, the width of enhanced swelling region would be controlled by He-containing bubbles rather than voids. This is because the presence of a high helium content in irradiated materials typically promotes the formation of He bubbles.

4.3. Broadening of the implanted ion profiles by radiation-enhanced diffusion (RED)

Although it is well known that implanted ions can suppress cavity swelling, there is a lack of detailed studies on RED broadening of the implanted ion profiles and its implications on microstructure evolution. Previous work [50] showed a significant variation in estimated RED values ranging from 10^{-20} to 10^{-17} m^2/s, for comparable high dose rate ion irradiation conditions. In the present study, the best fit ofD_{max} = 5 × 10^{-18} m^2/s is near the upper end of this range of RED values (Fig. 10). At 550 °C, the fitted D_{max} value of ~ 5 × 10^{-18} m^2/s using Eq. (1) and experimental estimates is ~ 4 times smaller than the D_{rad} value of ~ 2 × 10^{-17} m^2/s (Fig. A.3) calculated by Eq. (2) from kinetic rate theory equations for a surviving defect fraction of 100% NRT-dpa (equations and parameters used for the calculation can be found in the supplemental file). However, considering a surviving defect fraction of ~ 10% NRT-dpa [114] for irradiations where both interstitials and vacancies are mobile would decrease the D_{rad} value to ~ 6 × 10^{-18} m^2/s at 550 °C. The calculated D_{rad} with diffusivity (~6 × 10^{-18} m^2/s) comparable to the experimental fitted D_{max} value

Table 4
Calculated defect sink strength in neutron irradiated Cu and Cu-B alloy. Asterisks mark the irradiation temperatures where enhanced swelling regions were observed in Cu. (SFT: stacking fault tetrahedra).

Temperature (°C)	Cu		Cu-B alloy	
	Void (m^{-2})	Dislocation loop (m^{-2})	Void + bubble(m^{-2})	Dislocation loop + SFT (m^{-2})
250	5.5×10^{13}	1.4×10^{13}	2.0×10^{14}	1.1×10^{15}
275*	3.8×10^{13}	9.6×10^{12}	–	–
300*	3.7×10^{13}	9.2×10^{12}	–	–
350*	2.7×10^{13}	5.9×10^{12}	8.9×10^{13}	2.4×10^{13}

($\sim 5 \times 10^{-18}$) supports the suggestion in Ref [50] that the low reported D_{rad} values (10^{-20}-10^{-19} m^2/s) from some prior low-energy (<1 MeV) ion irradiation studies might be affected by surface sink effects.

According to Figs. 8 and 10, it is likely that implanted Ni ions can induce excessive injected interstitial effects on cavity swelling [43,59,60]. However, even for self-ion (using the same element for bombarding ion and target material) irradiation studies, the potential impact of diffusional broadening of the implanted ions should not be overlooked, especially when using low energy ions to produce very high displacement damage. Because radiation enhanced- and thermal-diffusion can both broaden the implanted ion profile (which is not considered in SRIM) and reduce the safe analysis region, it is suggested that a buffer zone between the safe analysis region and the SRIM estimated implanted ion band is generally needed to avoid the broadening of implanted ion profile during high dose irradiation studies at temperatures relevant for void swelling (particularly for irradiation temperatures > $0.45T_M$). This would narrow down the extent of the safe analysis region. In addition, implanting ion species distinct from the target material elements (e.g., Ni ions in Fe alloys) can cause potential chemical effects that could lead to more pronounced suppression of cavity swelling compared to self-ion injected interstitials. However, within the midrange of the analyzed Fe-Cr samples in this study, there was no evidence of nickel-containing precipitates or significant Ni solute concentration, based on STEM Z-contrast images or EDS/EELS elemental mapping [22,56]. From a different perspective, the use of dissimilar ions (rather than traditional "self-ions") can be beneficial to experimentally quantify radiation enhanced diffusion values vs. temperature and dose rate in a variety of materials (in order to provide additional high quality experimental measurements of RED).

4.4. Evolution of observable cavity swelling safe analysis zones at elevated temperatures

Cavity swelling typically increases with increasing dose [111]. For ion irradiation studies, as detailed in SRIM calculations, the dose (and dose rate) steadily increases with increasing depth within the midrange irradiated region. Therefore, in the safe analysis region, cavity swelling would be expected to increase with increasing depth. However, in Fig. 8a, a monotonic increase in swelling with increasing depth within the safe analysis region was not clear for the two 0.01 appm He/dpa samples irradiated at higher irradiation temperatures (500 and 550 °C). An enhanced swelling region near the surface was also not evident in the two samples irradiated at higher temperatures. Although the sub-grains observed in these samples [22] may artificially affect the swelling depth profile, these results infer that the extent of the safe analysis region could be reduced at relatively higher temperatures. Therefore, even when using an 8 MeV ion energy, a more pronounced diffusion of the injected ions and an increase of the cavity denuded zone width from the deep and shallow ends, respectively could narrow the safe analysis region to an unacceptably small value.

In addition, since the grain boundary in Fig. 9 is almost perpendicular to the sample surface, the predicted grain boundary cavity denuded zone should be proportional to $G^{-1/4}$ (for recombination dominant kinetics, cf. Eq (4)). In Fig. 15, the grain boundary cavity denuded zone width as a function of $G^{-1/4}$ from Fig. 9 shows a variety of slopes (indicated by red-dashed lines) in three depth ranges. In Fig. 15, the dashed lines indicate the lines that have been fitted to the data. The three ranges are in accordance with the surface-affected (0–750 nm), safe-analysis (750–1250 nm), and implanted ion-affected regions (1250–1750 nm), as shown in Fig. 8. In the two regions with artifacts, Eq. (4) may no longer be valid, and vacancy migration energy could not be accurately estimated by the cavity denuded zone width. This also highlights the importance of using higher ion energies. Traditional rate theory models may only be available for experimental ion-irradiation results collected from a "safe" depth range.

Fig. 16 illustrates a schematic of the safe analysis zone between the broadening of the injected ion-affected region and the temperature-dependent surface-affected region (including cavity denuded zone and enhanced swelling zone). The purple curves in Fig. 16 demonstrate the injected Ni ion profile in Fe target. As discussed earlier, our previous EDS line scan measurement [22] of the injected Ni profile showed that the peak position of the 8 MeV implanted Ni ions was ~ 700 nm less than the depth estimated by SRIM. Therefore, a correction factor of 1.5 was used to correct the peak position to match the 8 MeV Ni ion range measured by EDS. The peak of the corrected profile of 8 MeV Ni in Fe agrees well

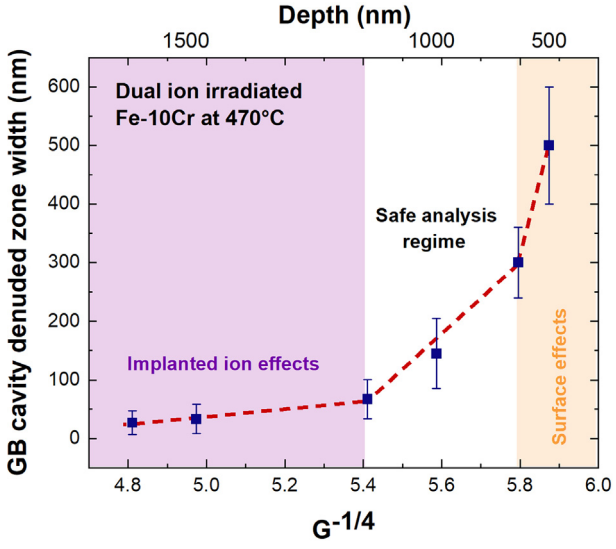

Fig. 15. Grain boundary cavity denuded zone width as a function of dose rate (G) in dual ion irradiated Fe-10Cr at 470 °C. The dashed lines represent the lines fitted to the data.

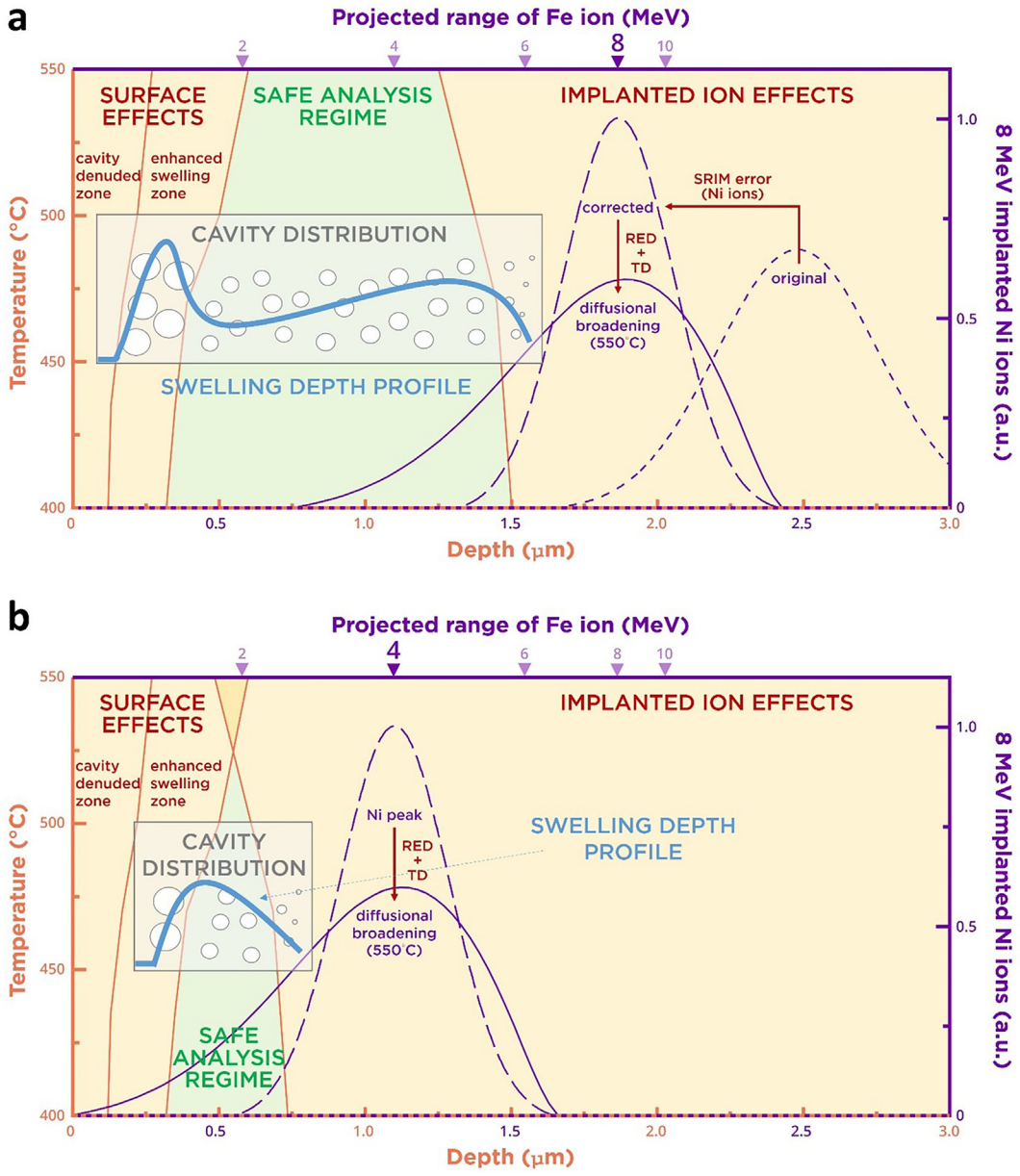

Fig. 16. Schematic diagrams of the surface and implanted ion effects on cavity swelling depth profile for Fe irradiated with (a) 8 MeV and (b) 4 MeV Ni ions, at midrange doses of 30 dpa and dose rates $\sim 1.4 \times 10^{-3}$ dpa/s.

with SRIM calculated range for 8 MeV Fe in Fe. In the same figure, with increasing temperature, both the surface-affected region and injected ion-affected region extend toward the safe analysis zone. An enhanced swelling zone may not be observed in every irradiated sample. In this study, such a peak swelling zone was only observed in samples with relatively low irradiation temperatures and lower total sink strength ($<10^{14}$ m^{-2}). If the enhanced swelling zone is present and if sufficiently high incident ion energies are used, the cavity swelling depth profile (blue curve) would have two peaks, as shown in Fig. 16a. The first peak adjacent to the cavity denuded zone is due to the enhanced swelling associated with preferential loss of 1D gliding interstitial clusters to the free surface. For the second peak near the midrange, the onset of the peak is naturally expected due to the increase of dose with depth, while the cessation of the peak is related to the injected ion effects (chemical or excessive interstitial effects) that suppress the cavity swelling.

Li et al. [112] recently reported a quantitative method to determine a region not influenced by injected interstitial and surface effects for void swelling analysis. However, the method was developed based on 1–5 MeV self-ion irradiation experiments, which may have prevented their study from observing a valid "safe analysis zone". If using a relatively lower incident ion energy (e.g., 4 MeV Fe ions in Fe, as shown in Fig. 16b), even at relatively low temperatures, it would be difficult to tell whether an enhanced swelling zone is present or not from a single peak. In this case, the observer could unconsciously consider the enhanced swelling zone to be part of the safe analysis zone. Therefore, higher ion energies (>8 MeV) are generally recommended to provide a relatively broad safe analysis region to separate the overlap of the injected ion-affected and surface-affected regions for well-controlled studies on irradiation effects. However, very high ion energies (>15 MeV) depending on the ion species and target material) should be avoided to minimize potential artifacts from swift

heavy ion effects [113]. In order to accurately assess the suitability of ion energies below 8 MeV for ion irradiation studies, it is important to carefully consider the near-surface and injected ion effects. These effects can vary depending on the combination of the injected ion and the target material, and may become more significant at high temperatures. Even when using ion energies above 8 MeV, the near-surface and injected ion effects can still decrease the safe analysis region. To ensure reliable results, it is crucial to take these effects into account in any ion irradiation conditions.

5. Conclusions

The near-surface (or grain boundary) cavity swelling phenomena (denuded zones and adjacent peak swelling zones) and diffusional broadening of implanted ions were investigated in neutron irradiated Cu and Ni, and dual-ion (Ni + He) irradiated Fe-Cr alloys. Theoretical models were used to examine the experimental results to construct an explanation for the formation of several unwanted artifacts and their potential effect on cavity swelling. The conclusions drawn from this work are as follows:

(i) For recombination-dominant conditions, the temperature dependence on cavity denuded zone width occurring next to planar surface or grain boundary sinks can be used to quantitatively estimate vacancy migration energies. However, this experimental method requires a relatively high density of cavities and a large number of data points in order to minimize statistical errors.
(ii) With the addition of helium (by neutron transmutation or co-injected He), bubble denuded zones were observed with a characteristic width less than the void denuded zones. This phenomenon is likely due to the formation of He-vacancy complexes with higher migration energy, which leads to a smaller cavity denuded zone width.
(iii) The formation of enhanced cavity swelling regions (or peak swelling zones) immediately adjacent to the cavity denuded zones may be related to the 1D glide of interstitial clusters. These peak swelling zones appear to be suppressed for high sink strengths ($>10^{14}$ m^{-2}), suggesting that high sink strength could suppress the 1D migration of interstitial clusters.
(iv) Injected ions can suppress cavity swelling with excessive interstitial and/or chemical effects. On top of this, radiation-enhanced diffusion together with thermal diffusion can broaden the implanted ion profile (extend the breadth of the injected ion-affected region) and thereby reduce the extent of the midrange safe analysis region.
(v) Dissimilar ion implantations with multi-MeV energies can be used to measure diffusional broadening and thereby accurately determine radiation enhanced diffusion parameters as a function of temperature and dose rate in a variety of materials.
(vi) The enhanced cavity swelling and implanted ion regions can partially overlap and therefore be difficult to detect when using low incident ion energies. This can lead to unconscious (incorrect) assumptions regarding the existence of a safe analysis region. Adequate ion energies (~8–15 MeV) are needed to provide a sufficiently broad safe analysis region for radiation effects studies.

CRediT authorship contribution statement

Yan-Ru Lin: Conceptualization, Methodology, Software, Formal analysis, Investigation, Data curation, Writing – original draft, Visualization. **Arunodaya Bhattacharya:** Resources, Writing – review & editing. **Steven J. Zinkle:** Conceptualization, Writing – review & editing, Supervision, Project administration, Funding acquisition.

Data availability

Data will be made available on request.

Declaration of Competing Interest

The authors declare that they have no known competing financial interests or personal relationships that could have appeared to influence the work reported in this paper.

Acknowledgements

We acknowledge Mao-Yuan Luo and E-Wen Huang for their assistance with SIMS analysis, which was supported by National Yang Ming Chiao Tung University, Taiwan. We thank Dr. Peter Doyle for providing the MATLAB routines for the radiation enhanced diffusion modeling. We thank Drs. Roger Stoller, Brian Wirth, William Weber, and Haixuan Xu for their insightful comments and suggestions.

Funding: This research was sponsored by the Office of Fusion Energy Sciences, U.S. Department of Energy under grant # DE-SC0006661 with the University of Tennessee (YRL and SJZ) and contract DE-AC05-00OR22725 with UT-Battelle, LLC (AB and SJZ). The fabrication of the Fe-Cr binary alloys has been carried out within the framework of the EUROfusion Consortium and has received funding from the Euratom research and training program 2019–2020 under Grant Agreement No. 633053. The authors would also like to acknowledge funding from the State of Tennessee and Tennessee Higher Education Commission (THEC) through their support of the Center for Materials Processing.

Appendix A. Supplementary material

Supplementary data to this article can be found online at https://doi.org/10.1016/j.matdes.2023.111668.

References

[1] H. Mehrer, Diffusion in Solids: Fundamentals, Methods, Materials, Diffusion-Controlled Processes, Springer Berlin Heidelberg, 2007.
[2] G.S. Was, Point Defect Formation and Diffusion, in: G.S. Was (Ed.), Fundamentals of Radiation Materials Science: Metals and Alloys, Springer, New York, New York, NY, 2017, pp. 167–205.
[3] Y.-R. Lin, A. Bhattacharya, D. Chen, Y. Zhao, J.-J. Kai, J. Henry, S.J. Zinkle, The role of Cr concentration and temperature on cavity swelling with co-injected helium in dual-ion irradiated Fe and Fe-Cr alloys, Mater. Des. 223 (2022) 111134.
[4] N. Daghbouj, H.S. Sen, J. Čížek, J. Lorinčík, M. Karlík, M. Callisti, J. Čech, V. Havránek, B. Li, V. Krsjak, M.O. Liedke, M. Butterling, A. Wagner, T. Polcar, Characterizing heavy ions-irradiated Zr/Nb: structure and mechanical properties, Mater. Des. 219 (2022) 110732.
[5] R. Ishikawa, R. Mishra, A.R. Lupini, S.D. Findlay, T. Taniguchi, S.T. Pantelides, S. J. Pennycook, Direct observation of dopant atom diffusion in a bulk semiconductor crystal enhanced by a large size mismatch, Phys. Rev. Lett. 113 (15) (2014) 155501.
[6] Y. Yang, H. Zhu, L. Wang, Y. Jiang, T. Wang, C. Liu, B. Li, W. Tang, Z. Wu, Z. Yang, D. Li, In-depth investigation of low-energy proton irradiation effect on the structural and photoresponse properties of ε-Ga2O3 thin films, Mater. Des. 221 (2022) 110944.
[7] T. Takagi, Ion beam modification of solids: towards intelligent materials, Mater. Sci. Eng. A 253 (1) (1998) 30–41.
[8] K.L. Firestein, D.G. Kvashnin, A.N. Sheveyko, I.V. Sukhorukova, A.M. Kovalskii, A.T. Matveev, O.I. Lebedev, P.B. Sorokin, D. Golberg, D.V. Shtansky, Structural analysis and atomic simulation of Ag/BN nanoparticle hybrids obtained by Ag ion implantation, Mater. Des. 98 (2016) 167–173.
[9] E. Recknagel, T. Wichert, Defects in metals studied by implanted radioactive atoms, Nucl. Inst. Methods 182–183 (1981) 439–455.
[10] G.S. Was, S.J. Zinkle, 1.14 - Toward the Use of Ion Irradiation to Predict Reactor Irradiation Effects, in: R.J.M. Konings, R.E. Stoller (Eds.),

Comprehensive Nuclear Materials (Second Edition), Elsevier, Oxford, 2020, pp. 468–484.
[11] S.J. Zinkle, L.L. Snead, Opportunities and limitations for ion beams in radiation effects studies: bridging critical gaps between charged particle and neutron irradiations, Scr. Mater. 143 (2018) 154–160.
[12] G.S. Was, Challenges to the use of ion irradiation for emulating reactor irradiation, J. Mater. Res. 30 (9) (2015) 1158–1182.
[13] L. Shao, J. Gigax, D. Chen, H. Kim, F.A. Garner, J. Wang, M.B. Toloczko, Standardization of accelerator irradiation procedures for simulation of neutron induced damage in reactor structural materials, Nucl. Instrum. Methods Phys. Res., Sect. B 409 (2017) 251–254.
[14] S. Taller, D. Woodley, E. Getto, A.M. Monterrosa, Z. Jiao, O. Toader, F. Naab, T. Kubley, S. Dwaraknath, G.S. Was, Multiple ion beam irradiation for the study of radiation damage in materials, Nucl. Instrum. Methods Phys. Res., Sect. B 412 (2017) 1–10.
[15] E. Getto, Z. Jiao, A.M. Monterrosa, K. Sun, G.S. Was, Effect of irradiation mode on the microstructure of self-ion irradiated ferritic-martensitic alloys, J. Nucl. Mater. 465 (2015) 116–126.
[16] J.G. Gigax, E. Aydogan, T. Chen, D. Chen, L. Shao, Y. Wu, W.Y. Lo, Y. Yang, F.A. Garner, The influence of ion beam rastering on the swelling of self-ion irradiated pure iron at 450 °C, J. Nucl. Mater. 465 (2015) 343–348.
[17] E.P. Simonen, N.M. Ghoniem, N.H. Packan, Pulsed flux effects on radiation damage, J. Nucl. Mater. 122 (1) (1984) 391–401.
[18] Standard Practice for Neutron Radiation Damage Simulation by Charged-Particle Irradiation, ASTM E 521, 2017, p. 20.
[19] W.G. Johnston, J.H. Rosolowski, A.M. Turkalo, T. Lauritzen, Nickel-ion bombardment of annealed and cold-worked type 316 stainless steel, J. Nucl. Mater. 48 (3) (1973) 330–338.
[20] J. Seran, J. Dupouy, The swelling of solution annealed 316 cladding in Rapsodie and Phenix, ASTM STP 782 (1982) 5–16.
[21] T. Okita, T. Sato, N. Sekimura, F.A. Garner, L.R. Greenwood, The primary origin of dose rate effects on microstructural evolution of austenitic alloys during neutron irradiation, J. Nucl. Mater. 307–311 (2002) 322–326.
[22] Y.-R. Lin, A. Bhattacharya, D. Chen, J.-J. Kai, J. Henry, S.J. Zinkle, Temperature-dependent cavity swelling in dual-ion irradiated Fe and Fe-Cr ferritic alloys, Acta Mater. 207 (2021) 116660.
[23] N.H. Packan, K. Farrell, J.O. Stiegler, Correlation of neutron and heavy-ion damage: I. The influence of dose rate and injected helium on swelling in pure nickel, J. Nucl. Mater. 78 (1) (1978) 143–155.
[24] L.K. Mansur, Correlation of neutron and heavy-ion damage: II. The predicted temperature shift if swelling with changes in radiation dose rate, J. Nucl. Mater. 78 (1) (1978) 156–160.
[25] S.J. Zinkle, L.L. Snead, Microstructure of copper and nickel irradiated with fission neutrons near 230°C, J. Nucl. Mater. 225 (1995) 123–131.
[26] M. Kiritani, Electron radiation damage of metals and nature of point defects by high voltage electron microscopy, in: Y.F. Robinson MT, Jr. (Ed.) Fundamental Aspects of Radiation Damage in Metals, Vol. II, Springfield, VA, CONF-751006-P2, 1975, pp. 695-714.
[27] D. Xu, A. Certain, H.-J.-L. Voigt, T. Allen, B.D. Wirth, Ballistic effects on the copper precipitation and re-dissolution kinetics in an ion irradiated and thermally annealed Fe–Cu alloy, J. Chem. Phys. 145 (10) (2016) 104704.
[28] O. Tissot, C. Pareige, E. Meslin, B. Decamps, J. Henry, Kinetics of α′ precipitation in an electron-irradiated Fe15Cr alloy, Scr. Mater. 122 (2016) 31–35.
[29] L.K. Mansur, Theory and experimental background on dimensional changes in irradiated alloys, J. Nucl. Mater. 216 (1994) 97–123.
[30] F.K. Naehring, A. Schmidt, J. Schöneich, Ion induced carbon contamination and recoil implantation, physica status solidi (a) 44(2) (1977) K141-K145.
[31] J. Wang, M.B. Toloczko, K. Kruska, D.K. Schreiber, D.J. Edwards, Z. Zhu, J. Zhang, Carbon contamination during ion irradiation - accurate detection and characterization of its effect on microstructure of ferritic/martensitic steels, Sci. Rep. 7 (1) (2017) 15813.
[32] M.J.F. Healy, Minimising carbon contamination during ion beam analysis, Nucl. Instrum. Methods Phys. Res., Sect. B 129 (1) (1997) 130–136.
[33] G.S. Was, S. Taller, Z. Jiao, A.M. Monterrosa, D. Woodley, D. Jennings, T. Kubley, F. Naab, O. Toader, E. Uberseder, Resolution of the carbon contamination problem in ion irradiation experiments, Nucl. Instrum. Methods Phys. Res., Sect. B 412 (2017) 58–65.
[34] K. Jin, C. Lu, L.M. Wang, J. Qu, W.J. Weber, Y. Zhang, H. Bei, Effects of compositional complexity on the ion-irradiation induced swelling and hardening in Ni-containing equiatomic alloys, Scr. Mater. 119 (2016) 65–70.
[35] S.J. Zinkle, Anisotropic dislocation loop nucleation in ion-irradiated MgAl2O4, J. Nucl. Mater. 191–194 (1992) 645–649.
[36] D.S. Gelles, F.A. Garner, H.R. Brager, Frank Loop Formation in Irradiated Metals in Response to Applied and Internal Stresses, in: B.H. Kramer D, Perrin JS (Ed.) 10th Int. Symp. on Effects of Radiation on Materials, ASTM STP 725. American Society for Testing and Materials, Philadelphia, 1981, pp. 735–753.
[37] H. Trinkaus, B.N. Singh, A.J.E. Foreman, Impact of glissile interstitial loop production in cascades on defect accumulation in the transient, J. Nucl. Mater. 206 (2) (1993) 200–211.
[38] O. El-Atwani, J.E. Nathaniel, A.C. Leff, J.K. Baldwin, K. Hattar, M.L. Taheri, Evidence of a temperature transition for denuded zone formation in nanocrystalline Fe under He irradiation, Mater. Res. Lett. 5 (3) (2017) 195–200.
[39] M.J. Makin, A simple theory of loop formation and enhanced diffusion in crystals examined by high voltage electron microscopy, Philos. Mag.: J. Theoret. Exp. Appl. Phys. 20 (168) (1969) 1133–1146.
[40] K. Farrell, J.T. Houston, Heterogeneous distribution of irradiation voids in iron, J. Nucl. Mater. 35 (3) (1970) 352–355.
[41] J.A. Hudson, D.J. Mazey, R.S. Nelson, Void formation in nickel during 20 MeV C ++ irradiation at 525 °C, J. Nucl. Mater. 41 (3) (1971) 241–256.
[42] C.W. Chen, R.W. Buttry, Void formation and denudation in ion-irradiated nickel, Radiat. Eff. Defects Solids 56 (3–4) (1981) 219–228.
[43] J.B. Whitley, G.L. Kulcinski, P. Wilkes, H.V. Smith, The depth dependent damage profile in nickel irradiated with nickel or copper ions, J. Nucl. Mater. 79 (1) (1979) 159–169.
[44] E.H. Lee, L.K. Mansur, M.H. Yoo, Spatial variation in void volume during charged particle bombardment — the effects of injected interstitials, J. Nucl. Mater. 85–86 (1979) 577–581.
[45] F.A. Garner, Impact of the injected interstitial on the correlation of charged particle and neutron-induced radiation damage, J. Nucl. Mater. 117 (1983) 177–197.
[46] B. Badger, Jr., D.L. Plumton, S.J. Zinkle, R.L. Sindelar, G.L. Kulcinski, R.A. Dodd, W.G. Wolfer, Experimental investigation of the effect of injected interstitials on void formation, ASTM STP 870, Philadelphia, 1985, pp. 297-316.
[47] T.-N. Yang, C. Lu, K. Jin, M.L. Crespillo, Y. Zhang, H. Bei, L. Wang, The effect of injected interstitials on void formation in self-ion irradiated nickel containing concentrated solid solution alloys, J. Nucl. Mater. 488 (2017) 328–337.
[48] L.M. Wang, R.A. Dodd, G.L. Kulcinski, Radiation damage and copper distribution in 14 MeV copper-ion-implanted nickel — TEM and AEM analyses in cross-section, Ultramicroscopy 29 (1) (1989) 284–290.
[49] O. Tissot, C. Pareige, E. Meslin, B. Décamps, J. Henry, Influence of injected interstitials on α′ precipitation in Fe–Cr alloys under self-ion irradiation, Mater. Res. Lett. 5 (2) (2017) 117–123.
[50] P.J. Doyle, K.M. Benensky, S.J. Zinkle, Modeling the impact of radiation-enhanced diffusion on implanted ion profiles, J. Nucl. Mater. 509 (2018) 168–180.
[51] W.F. Cureton, C.L. Tracy, M. Lang, Review of swift heavy ion irradiation effects in CeO2, Quantum Beam Science 5 (2) (2021) 19.
[52] M. Lang, F. Djurabekova, N. Medvedev, M. Toulemonde, C. Trautmann, 1.15 - Fundamental Phenomena and Applications of Swift Heavy Ion Irradiations, in: R.J.M. Konings, R.E. Stoller (Eds.), Comprehensive Nuclear Materials (Second Edition), Elsevier, Oxford, 2020, pp. 485–516.
[53] P.J. Goodhew, Cavity growth mechanism maps, Scr. Metall. 18 (10) (1984) 1069–1073.
[54] S.J. Zinkle, K. Farrell, Void swelling and defect cluster formation in reactor-irradiated copper, J. Nucl. Mater. 168 (3) (1989) 262–267.
[55] S.J. Zinkle, K. Farrell, H. Kanazawa, Microstructure and cavity swelling in reactor-irradiated dilute copper-boron alloy, J. Nucl. Mater. 179–181 (1991) 994–997.
[56] Y.-R. Lin, Fundamentals of Cavity Formation in α-Fe and Fe-Cr Alloys, University of Tennessee, Knoxville, PhD thesis, 2021.
[57] L.K. Mansur, Void swelling in metals and alloys under irradiation: an assessment of the theory, Nucl. Technol. 40 (1) (1978) 5–34.
[58] S.J. Zinkle, Microstructure of ion irradiated ceramic insulators, Nucl. Instrum. Methods Phys. Res., Sect. B 91 (1) (1994) 234–246.
[59] D.L. Plumton, W.G. Wolfer, Suppression of void nucleation by injected interstitials during heavy ion bombardment, J. Nucl. Mater. 120 (2) (1984) 245–253.
[60] D.L. Plumton, G.L. Kulcinski, The magnitude and distribution of the excess interstitial fraction during heavy ion irradiation, J. Nucl. Mater. 133–134 (1985) 444–447.
[61] X. Shu, W. Chongyu, Self-diffusion of Fe and diffusion of Ni in Fe calculated with MAEAM theory, Phys. B Condens. Matter 344 (1) (2004) 413–422.
[62] S.L. Dudarev, Density functional theory models for radiation damage, Annu. Rev. Mat. Res. 43 (1) (2013) 35–61.
[63] K. Hirano, M. Cohen, B.L. Averbach, Diffusion of nickel into iron, Acta Metall. 9 (5) (1961) 440–445.
[64] W. Han, M. Demkowicz, E. Fu, Y. Wang, A. Misra, Effect of grain boundary character on sink efficiency, Acta Mater. 60 (2012) 6341–6351.
[65] Y.V. Konobeev, A.V. Subbotin, V.N. Bykov, V.I. Tscherbak, Grain boundary void denuded zone in irradiated metals, Phys. Stat. Sol. 29 (1975) K121.
[66] J.L. Brimhall, B. Mastel, Stability of voids in neutron irradiated nickel, J. Nucl. Mater. 33 (2) (1969) 186–194.
[67] D.I.R. Norris, The use of the high voltage electron microscope to simulate fast neutron-induced void swelling in metals, J. Nucl. Mater. 40 (1) (1971) 66–76.
[68] Y.V. Konobeev, V.I. Tscherbak, V.N. Bykov, A.V. Subbotin, Determination of the Vacancy Diffusivity in Molybdenum and Nickel from Data on the Width of the Grain Boundary Void Denuded Zone, physica status solidi (a) 40(2) (1977) K89-K92.
[69] Y. Sekio, S. Yamashita, N. Sakaguchi, H. Takahashi, Void denuded zone formation for Fe–15Cr–15Ni steel and PNC316 stainless steel under neutron and electron irradiations, J. Nucl. Mater. 458 (2015) 355–360.
[70] B.N. Singh, Effect of grain size on void formation during high-energy electron irradiation of austenitic stainless steel, Philos. Mag.: J. Theoret. Exp. Appl. Phys. 29 (1) (1973) 25–42.
[71] S. Zinkle, Dislocation loop Formation in ion-irradiated Polycrystalline Spinel and Alumina, ASTM STP 1125 (1992) 749–763.

[72] A.J.E. Foreman, The diffusion of point defects to the foil surface during irradiation damage experiments in the high voltage electron microscope, Radiat. Eff. Defects Solids 14 (3–4) (1972) 175–179.
[73] N.Q. Lam, S.J. Rothman, R. Sizmann, Steady-state point-defect diffusion profiles in solids during irradiation, Radiat. Eff. Defects Solids 23 (1) (1974) 53–59.
[74] W.Z. Han, M.J. Demkowicz, E.G. Fu, Y.Q. Wang, A. Misra, Effect of grain boundary character on sink efficiency, Acta Mater. 60 (18) (2012) 6341–6351.
[75] W.G. Wolfer, 1.01 - Fundamental Properties of Defects in Metals, in: R.J.M. Konings (Ed.), Comprehensive Nuclear Materials, Elsevier, Oxford, 2012, pp. 1–45.
[76] R.W. Balluffi, Vacancy defect mobilities and binding energies obtained from annealing studies, J. Nucl. Mater. 69–70 (1978) 240–263.
[77] S.J. Zinkle, B.N. Singh, Microstructure of Cu–Ni alloys neutron irradiated at 210°C and 420°C to 14 dpa, J. Nucl. Mater. 283–287 (2000) 306–312.
[78] M. Hatakeyama, H. Watanabe, M. Akiba, N. Yoshida, Low void swelling in dispersion strengthened copper alloys under single-ion irradiation, J. Nucl. Mater. 307–311 (2002) 444–449.
[79] S.J. Zinkle, N. Hashimoto, D.T. Hoelzer, A.L. Qualls, T. Muroga, B.N. Singh, Effect of periodic temperature variations on the microstructure of neutron-irradiated metals, J. Nucl. Mater. 307–311 (2002) 192–196.
[80] C. González, R. Iglesias, Migration mechanisms of helium in copper and tungsten, J. Mater. Sci. 49 (23) (2014) 8127–8139.
[81] A.Y. Dunn, M.G. McPhie, L. Capolungo, E. Martinez, M. Cherkaoui, A rate theory study of helium bubble formation and retention in Cu–Nb nanocomposites, J. Nucl. Mater. 435 (1) (2013) 141–152.
[82] P. Jung, K. Schroeder, Diffusion and agglomeration of helium in FCC metals, J. Nucl. Mater. 155–157 (1988) 1137–1141.
[83] J.A. Sprague, J.E. Westmoreland, F.A. Smidt, P.R. Malmberg, The temperature dependence of nickel-ion damage in nickel, J. Nucl. Mater. 54 (2) (1974) 286–298.
[84] J.E. Westmoreland, J.A. Sprague, F.A. Smidt, P.R. Malmberg, Dose rate effects in nickel-ion-irradiated nickel, Radiat. Eff. Defects Solids 26 (1–2) (1975) 1–16.
[85] M.A. Shaikh, Void denudation and grain boundary migration in ion-irradiated nickel, J. Nucl. Mater. 187 (3) (1992) 303–306.
[86] E.H. Megchiche, C. Mijoule, M. Amarouche, First principles calculations of vacancy–vacancy interactions in nickel: thermal expansion effects, J. Phys. Condens. Matter 22 (48) (2010) 485502.
[87] S. Mahmoud, M. Trochet, O.A. Restrepo, N. Mousseau, Study of point defects diffusion in nickel using kinetic activation-relaxation technique, Acta Mater. 144 (2018) 679–690.
[88] C. Allard, G.S. Collins, C. Hohenemser, Vacancy migration and accretion in Ni observed by perturbed γ-γ angular correlations, Phys. Rev. B 32 (8) (1985) 4839–4848.
[89] F.A. Garner, L.E. Thomas, Production of Voids in Stainless Steel by High-Voltage Electrons, in: J. Moteff (Ed.), Effects of radiation on substructure and mechanical properties of metals and alloys, ASTM STP 529, Philadelphia, 1973, pp. 303–323.
[90] M.B. Lewis, Diffusion and trapping of ion-implanted helium in nickel, J. Nucl. Mater. 149 (2) (1987) 143–149.
[91] A.J. Adams, W.G. Wolfer, On the diffusion mechanisms of helium in nickel, J. Nucl. Mater. 158 (1988) 25–29.
[92] G.L. Kulcinski, B. Mastel, H.E. Kissinger, Characterization and annealing behavior of voids in neutron-irradiated nickel, Acta Metall. 19 (1) (1971) 27–36.
[93] D. Costa, G. Adjanor, C.S. Becquart, P. Olsson, C. Domain, Vacancy migration energy dependence on local chemical environment in Fe–Cr alloys: a density functional theory study, J. Nucl. Mater. 452 (1) (2014) 425–433.
[94] C.-C. Fu, J.D. Torre, F. Willaime, J.-L. Bocquet, A. Barbu, Multiscale modelling of defect kinetics in irradiated iron, Nat. Mater. 4 (1) (2005) 68–74.
[95] F. Gao, H.L. Heinisch, R.J. Kurtz, Migration of vacancies, He interstitials and He-vacancy clusters at grain boundaries in α-Fe, J. Nucl. Mater. 386–388 (2009) 390–394.
[96] C.-C. Fu, F. Willaime, Ab initio study of helium in α-Fe: dissolution, migration, and clustering with vacancies, Phys. Rev. B 72 (6) (2005) 064117.
[97] D. Kaoumi, A.T. Motta, R.C. Birtcher, A thermal spike model of grain growth under irradiation, J. Appl. Phys. 104 (7) (2008) 073525.
[98] A.D. Brailsford, L.K. Mansur, Effect of self-ion injection in simulation studies of void swelling, J. Nucl. Mater. 71 (1) (1977) 110–116.
[99] J.O. Stiegler, E.E. Bloom, Void formation in irradiated Nickel 270, Radiat. Eff. Defects Solids 8 (1–2) (1971) 33–41.
[100] A.J.E. Foreman, B.N. Singh, A. Horsewell, Diffusion mechanisms for enhanced vacancy accumulation near planar sinks, Mater. Sci. Forum 15–18 (1987) 895–900.
[101] C.A. Dennett, K.P. So, A. Kushima, D.L. Buller, K. Hattar, M.P. Short, Detecting self-ion irradiation-induced void swelling in pure copper using transient grating spectroscopy, Acta Mater. 145 (2018) 496–503.
[102] S.I. Porollo, A.M. Dvoriashin, Y.V. Konobeev, F.A. Garner, Microstructure and swelling of neutron irradiated nickel and binary nickel alloys, J. Nucl. Mater. 442 (1, Supplement 1) (2013) S809–S812.
[103] H. Kim, J.G. Gigax, J. Fan, F.A. Garner, T.L. Sham, L. Shao, Swelling resistance of advanced austenitic alloy A709 and its comparison with 316 stainless steel at high damage levels, J. Nucl. Mater. 527 (2019) 151818.
[104] Z. Fan, W. Zhong, K. Jin, H. Bei, Y.N. Osetsky, Y. Zhang, Diffusion-mediated chemical concentration variation and void evolution in ion-irradiated NiCoFeCr high-entropy alloy, J. Mater. Res. 36 (1) (2021) 298–310.
[105] T. Wang, H. Kim, F.A. Garner, K.L. Peddicord, L. Shao, The effect of internal free surfaces on void swelling of irradiated pure iron containing subsurface trenches, Crystals 9 (5) (2019) 252.
[106] M.A. Puigvi, Y.N. Osetsky, A. Serra, Point-defect clusters and dislocation loops in bcc metals: continuum and atomistic study, Phil. Mag. 83 (7) (2003) 857–871.
[107] Y.N. Osetsky, D.J. Bacon, B.N. Singh, B. Wirth, Atomistic study of the generation, interaction, accumulation and annihilation of cascade-induced defect clusters, J. Nucl. Mater. 307–311 (2002) 852–861.
[108] K. Arakawa, K. Ono, M. Isshiki, K. Mimura, M. Uchikoshi, H. Mori, Observation of the one-dimensional diffusion of nanometer-sized dislocation loops, Science 318 (5852) (2007) 956–959.
[109] L. Wang, D. Martin, W.-Y. Chen, P.M. Baldo, M. Li, B.D. Wirth, S.J. Zinkle, Effect of sink strength on coherency loss of precipitates in dilute Cu-base alloys during in situ ion irradiation, Acta Mater. 210 (2021) 116812.
[110] H. Trinkaus, B.N. Singh, M. Victoria, Microstructural evolution adjacent to grain boundaries under cascade damage conditions and helium production, J. Nucl. Mater. 233–237 (1996) 1089–1095.
[111] F.A. Garner, 4.02 - Radiation Damage in Austenitic Steels, in: R.J.M. Konings (Ed.), Comprehensive Nuclear Materials, Elsevier, Oxford, 2012, pp. 33–95.
[112] Y. Li, A. French, Z. Hu, A. Gabriel, L.R. Hawkins, F.A. Garner, L. Shao, A quantitative method to determine the region not influenced by injected interstitial and surface effects during void swelling in ion-irradiated metals, J. Nucl. Mater. 154140 (2022).
[113] Z.G. Wang, C. Dufour, E. Paumier, M. Toulemonde, The Se sensitivity of metals under swift-heavy-ion irradiation: a transient thermal process, J. Phys. Condens. Matter 6 (34) (1994) 6733–6750.
[114] S.J. Zinkle, R.E. Stoller, Quantifying defect production in solids at finite temperatures: Thermall y -activate d correlated defect recombination correction s to DP A (CRC -DPA), J. Nucl. Mater. 154292 (2023).